

The Warm-Hot Disk-Halo Interface Below the Perseus Spiral Arm*

ANANYA GOON TULI,¹ NICOLAS LEHNER,¹ J. CHRISTOPHER HOWK,¹ TODD M. TRIPP,² ANDREW J. FOX,³ AND FRANCES H. CASHMAN⁴

¹*Department of Physics and Astronomy, University of Notre Dame, Notre Dame, IN 46556*

²*Department of Astronomy, University of Massachusetts, Amherst, MA 01003-9305*

³*AURA for ESA, Space Telescope Science Institute, 3700 San Martin Drive, Baltimore, MD 21218*

⁴*Department of Physics, Presbyterian College, 503 South Broad Street, Clinton, SC 29325*

ABSTRACT

The Milky Way’s disk-halo interface mediates energy and mass exchange between the interstellar thin disk and the halo. In the first detailed study of the Perseus arm’s disk-halo interface, we combine HST/STIS and COS absorption spectra toward 6 stars and 23 AGNs projected behind a narrow section ($95^\circ < l < 145^\circ$, $-46^\circ < b < 0^\circ$), providing a unique dataset that bridges the disk and its extended vertical structure in these directions. We detect S II, Si IV, and C IV absorption, along with H I 21 cm emission, within -70 pc to -3.3 kpc from the mid-plane. The arm’s southern vertical structure exhibits complexity beyond simple exponential scaling: H I and S II column densities sharply decline with height up to 1.5 kpc before flattening, while high ion (Si IV and C IV) column densities remain relatively constant. In this region, where warm neutral medium (WNM) dominates, S II and the high ions show similar kinematics, and we find a remarkably uniform C IV/Si IV ratio ($\langle N_{\text{CIV}}/N_{\text{SiIV}} \rangle = 2.5 \pm 0.5$) within -0.9 to -3.25 kpc. Both the kinematic correspondence and high-ion ratio are consistent with the high ions probing turbulent mixing layers at the interfaces between warm/cool and hot gas phases. AGN sightlines reveal minimal circumgalactic medium (CGM) contribution in the low-velocity gas at $|v_{\text{LSR}}| < 100$ km s⁻¹, suggesting the observed properties may be attributed to previous fountain activity.

1. INTRODUCTION

The Milky Way’s spiral arms are loci of active star formation (McKee & Ostriker 2007; Elmegreen 2011). Within the spiral arms, spatially- and temporally-correlated feedback from stars (e.g., strong stellar winds and supernova explosions) evolve into super-bubbles that expand through the interstellar medium (ISM). Eventually, these super-bubbles break out as Galactic fountains (Shapiro & Field 1976; Bregman 1980) and chimneys (Norman & Ikeuchi 1989) when the hot ($T > 10^6$ K) gas escapes into the extraplanar regions above/below the spiral arms. This activity plays a crucial role in galaxy evolution: it is now widely recognized that the competition between *feedback* (driven by outflows and escaping ionizing light) vs. *accretion* (inflows of relatively pristine gas as well as recycled fountain material) regulates star formation (Thompson & Heckman 2024) and enables galaxies to continue to evolve over their lifetimes. The extraplanar disk-halo interface region, roughly within 5 kpc of the Galactic plane

(e.g., Bowen et al. 2008; Savage & Wakker 2009), is the linchpin of this “baryon cycle”: this is where outflowing matter, energy, and momentum are coupled with the broader surroundings of a galaxy, and conversely, this is the region that inflowing material must navigate to survive its descent into the disk, where it can eventually form new stars. The disk-halo interface thus connects the Milky Way’s interstellar thin disk (scale height ~ 200 – 300 pc, Ojha 2001) to the distant halo gas known as the circumgalactic medium (CGM) (Savage et al. 2003; Putman et al. 2009; Wakker et al. 2012).

The disk-halo interface is supported by the energy and matter of stellar feedback from the spiral arms (Heckman 2002; Kim & Ostriker 2018), which impacts the disk-halo interface’s large-scale density distribution and extension of various gas phases above the Galactic plane. The bulk transportation of matter from the spiral arms into the disk-halo interface through galactic fountains and chimneys sets the vertical extension of the arms as well as determines the ionization conditions in the extraplanar region. Moreover, the disk-halo interface facilitates the mixing of enriched feedback material with the falling pristine halo material (Putman et al. 2009), which must determine the chemical composition of the disk-halo interface gas. Therefore, the disk-halo interface’s gas distribution, extension, ionization condition,

* Based on observations made with the NASA/ESA Hubble Space Telescope, obtained from the data archive at the Space Telescope Science Institute. STScI is operated by the Association of Universities for Research in Astronomy, Inc. under NASA contract NAS 5-26555.

and chemical composition are important aspects of the Galactic structure and evolution.

Historically, the spatial structure of the nearby disk-halo interface gas has been characterized as a flat slab with an exponential density distribution (Lockman et al. 1986; Dickey & Lockman 1990; Savage & Massa 1985; Sembach & Savage 1992; Savage et al. 1997; Haffner et al. 1999; Savage et al. 2003; Bowen et al. 2008; Savage & Wakker 2009; Wakker et al. 2012). Using this simplified concept, the scale heights of the different disk-halo interface gas phases has been estimated, e.g., $h_z = 0.5$ kpc for the warm neutral medium (WNM) ($\leq 10^4$ K) (Lockman et al. 1986; Dickey & Lockman 1990), 1 kpc for the warm ionized medium (WIM) ($\sim 10^4$ – $10^{4.2}$ K) (Haffner et al. 1999; Krishnarao et al. 2017), and 3–4 kpc for the transition temperature phase between $\sim 10^{4.2}$ – $10^{5.5}$ K (Savage & Massa 1985; Sembach & Savage 1992; Savage et al. 1997, 2003; Bowen et al. 2008; Savage & Wakker 2009; Wakker et al. 2012).

Characterizing the spatial structure of the transition temperature phase in the disk-halo interface is particularly important since the hot feedback material cools through this phase. Si IV, C IV, N V, and O VI ions have some of the strongest transition lines in UV and provide significant cooling rates for the hot material, thus regulating the disk-halo interface’s physical conditions. The transition temperature ions’ column density distributions observed using halo star sightlines agree with the flat slab model fits (Bowen et al. 2008; Savage & Wakker 2009). However, column densities observed along a large sample of AGN sightlines significantly deviate from the flat-slab model fits (Zheng et al. 2019; Qu & Bregman 2019; Qu et al. 2020, 2022). Additionally, stellar feedback, e.g., Galactic fountains and chimneys, may substantially alter the gas distribution and ionization conditions above/below the spiral arms—a phenomenon yet unexplored. To resolve the observational tensions between the halo star and AGN sightlines as well as to evaluate stellar feedback’s impact on the disk-halo interface gas, we design an experiment investigating the extraplanar H I, S II, Si IV and C IV density distribution beneath the Perseus arm using H I 21 cm emission and UV spectra of OB stars and AGNs. The Perseus arm provides unique advantages: its proximity enables precise stellar distance measurements via *Gaia* parallaxes (Lindegren et al. 2021), and its kinematics facilitate unambiguous gas localization. Our methodology (Section 2) directly probes the vertical density distribution and ionization physics of extraplanar Perseus gas at the disk-halo interface, potentially illuminating galactic fountain dynamics.

This paper is organized as follows: Section 2 and Section 3 describe our experiment and the target selection process. In section 4, we discuss the data products and the analysis process. In Section 5, we present our results and discuss their implications in Section 6. Finally, we summarize our main findings in Section 7.

2. OUR EXPERIMENT

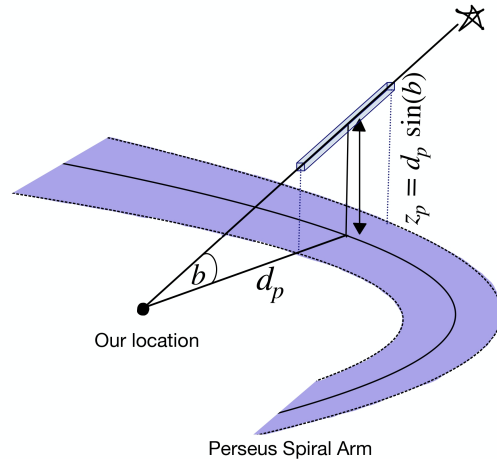


Figure 1. A schematic of our experiment. A sightline toward a target projected behind the Perseus arm passes above/below the Perseus arm at a specific mid-arm height $|z_P|$. Based on kinematics, we select the absorption associated with the extraplanar Perseus gas (the blue parallelogram) above/below the arm (see Section 4.5 and Table 2) and measure its column density (see Section 4.6 and Table 3). Therefore, we can estimate the column density vs. $|z_P|$ distribution using a sample of multiple sightlines (see Section 5.3 and Figure 7).

Figure 1 illustrates our experimental design for probing the vertical structure of the Perseus arm. We utilize absorption spectroscopy along sightlines toward background sources projected behind the Perseus arm. Each sightline intersects the arm’s extraplanar gas (depicted by the parallelogram), spanning a range of heights. The mid-arm height of the extraplanar gas (above/below the Galactic plane) along a sightline is $|z_P| = d_P \sin b$, where d_P is the mid-arm distance to the Perseus arm in the sightline’s direction, and b is the latitude of the sightline. This extraplanar gas imprints characteristic absorption features in the spectra of background sources. Knowing the gas kinematics (see Section 3), we can isolate Perseus absorption in these spectra to derive the associated column densities. Thus, using a set of background sources projected behind the Perseus arm and

Table 1. Sample Summary

Target	ID	l	b	Type	$D_{\text{star}}^{\text{a}}$	D_{P}^{b}	$ z_{\text{P}} ^{\text{c}}$	Instruments	S/N^{d}
		($^{\circ}$)	($^{\circ}$)		(kpc)	(kpc)	(kpc)		C IV/Si IV
BD+60 73	S1	121.22	-1.46	B1Ib	4.00 ($^{+0.20}_{-0.18}$)	2.60	0.07	STIS E140M	10/9
HD 14434	S2	135.08	-3.82	O5.5Vnn(f)p	2.52 ($^{+0.15}_{-0.14}$)	2.24	0.15	STIS E140M	62/49
HD 210809	S3	99.85	-3.13	O9Iab	4.33 ($^{+0.73}_{-0.54}$)	3.69	0.21	STIS E140H/E140M	84/21
HD 13745	S4	134.58	-4.96	O9.7II(n)	2.60 ($^{+0.19}_{-0.16}$)	2.25	0.21	STIS E140M	57/62
HD 232522	S5	130.70	-6.71	B1II	4.12 ($^{+0.74}_{-0.55}$)	2.33	0.27	STIS E140H	... /274
3C66A	A1	140.14	-16.77	AGN	...	2.15	0.65	COS G130M/G160M	7/11
Zw535.012	A2	120.17	-17.13	AGN	...	2.63	0.81	COS G130M/G160M	5/8
FBS0150+396	A3	135.58	-21.42	AGN	...	2.23	0.87	COS G130M/G160M	7/5
IRASF00040+4325	A4	114.42	-18.42	AGN	...	2.86	0.92	COS G130M/G160M	8/15
UVQSJ001903.85+423809.0	A5	116.61	-19.84	AGN	...	2.77	0.99	COS G130M/G160M	4/5
PGC2304	A6	120.34	-21.33	AGN	...	2.63	1.03	COS G130M/G160M	4/4
RXSJ0118.8+3836	A7	128.78	-23.95	AGN	...	2.38	1.06	COS G130M/G160M	5/5
IVZw29	A8	121.04	-22.51	AGN	...	2.60	1.08	COS G130M/G160M	11/12
RXJ0048.3+3941	A9	122.28	-23.18	AGN	...	2.56	1.11	COS G130M/G160M	16/6
RXJ0049.8+3931	A10	122.60	-23.35	AGN	...	2.55	1.11	COS G130M/G160M	8/60
LAMOSTJ003432.52+391836.1	A11	119.37	-23.44	AGN	...	2.66	1.15	COS G130M/G160M	4/6
RXSJ0155.6+3115	A12	138.70	-29.64	AGN	...	2.17	1.23	COS G130M/G160M	4/10
RXJ0043.6+3725	A13	121.23	-25.42	AGN	...	2.60	1.24	COS G130M/G160M	7/8
3C48.0	A14	133.96	-28.72	AGN	...	2.26	1.24	COS G130M/G160M	5/7
RXJ0050.8+3536	A15	122.80	-27.26	AGN	...	2.55	1.31	COS G130M/G160M	7/7
RXJ0028.1+3103	A16	117.09	-31.54	AGN	...	2.75	1.69	COS G130M/G160M	7/15
PG0052+251	A17	123.91	-37.44	AGN	...	2.51	1.92	COS G130M/G160M	8/18
PG0122+214	S6	133.37	-40.57	B2-3V	8.96 ($^{+6.06}_{-2.58}$)	2.27	1.94	STIS E140M	10/15
4C25.01	A18	114.07	-36.28	AGN	...	2.87	2.11	COS G130M/G160M	11/8
RXJ0053.7+2232	A19	123.64	-40.33	AGN	...	2.52	2.14	COS G130M/G160M	4/8
RBS2055	A20	106.67	-34.66	AGN	...	3.24	2.24	COS G130M/G160M	8/9
MRK1148	A21	123.09	-45.44	AGN	...	2.54	2.58	COS G130M/G160M	7/9
MRK335	A22	108.76	-41.42	AGN	...	3.13	2.76	COS G130M/G160M	14/15
PG0003+158	A23	107.32	-45.33	AGN	...	3.21	3.25	COS G130M/G160M	10/11

NOTE—(a): Distances to the stars with 68% confidence interval using Gaia parallaxes (Lindegren et al. 2021). (b): Distance to the Perseus arm in the direction of the target using the spiral arm equation and the parameters for the Perseus Arm in Table 2 of Reid et al. (2014). (c): mid-arm height $|z_{\text{P}}|$ below the Perseus arm. (d): Signal-to-noise ratio per resolution derived in the stellar continuum around the C IV and Si IV lines, respectively. Stellar spectral type references: Morgan et al. 1955; Walborn 1972; Walborn 1973; Humphreys 1978 Ramspeck et al. 2001; Maíz-Apellániz et al. 2004

passing above/below it at a range of $|z_{\text{P}}|$ values, we can probe the spatial structure and physical conditions in the arm’s vertical extension. We conduct this experiment over a narrow section of the Perseus arm where its spiral structure and gas kinematics are well understood (see Section 3), ensuring appropriate identification of the Perseus absorption toward each sightline and thus reliable characterization of the arm’s vertical structure.

Our experiment differs from previous multi-sightline surveys (e.g., Diplas & Savage 1994; Savage et al. 1997, 2003; Bowen et al. 2008; Savage & Wakker 2009; Wakker et al. 2012) in two fundamental ways. The first distinction lies in our column density selection method. While previous works measured the integrated total column

density (N) along the entire sightline, we use kinematic information to isolate and measure only the column density of the extraplanar Perseus arm gas. The second key difference is in our vertical distance metric. Earlier studies assessed the disk-halo interface gas distribution using sightlines through out the Galaxy, and measuring the total vertical column density ($N \sin b$) integrated up to the maximum height, z , of each sightline. Our approach, however, examines the column density associated with the Perseus arm at a specific $|z_{\text{P}}|$, the Perseus mid-arm height—that is we are measuring $N(z = z_{\text{P}})$ instead of $N(< z) = \int N(z) dz$. This allows us to assess the extension and ionization of the disk-halo interface gas focusing only on the extraplanar gas directly below a

narrow segment of the Perseus arm. These methodological differences enable a more targeted analysis of the Perseus arm’s southern vertical density structure and the physical properties in the gas.

3. TARGET SELECTION

We determined the optimal region for conducting our survey, using CO (Dame et al. 1987; Reid et al. 2016) and H I (Reid et al. 2016; Du et al. 2016) emission observations of the Perseus arm, alongside surveys of Galactic disk-halo interface H I clouds (e.g., Wakker 2001). We require both distances to *and* kinematics of the Perseus arm as a function of Galactic longitude to build a sample of targets where Perseus absorption can be robustly constrained. Caution must be exercised in associating ISM gas with individual spiral arms solely based on kinematics since small perturbations from Galactic rotation lead to incorrect association with distance in the outer Galaxy (Burton 1971; Peek et al. 2022). However, parallax-based distances to the high mass star forming regions (Reid et al. 2014) and OB associations (Xu et al. 2018) confirm a continuous spiral structure at the distance of the Perseus arm within $95^\circ \leq l \leq 140^\circ$. The detailed spiral structure, e.g., the heliocentric distance, arm width, and pitch angle, in this longitude range has been well-studied using both gas kinematics and parallax-based distances (Reid et al. 2009, 2014; Xu et al. 2018, 2023; Reid et al. 2019; Söding et al. 2024). Atomic and molecular line observations in the Galactic plane further show that the Perseus gas velocity range within $95^\circ \leq l \leq 140^\circ$ is well separated from the foreground and background gas. We, therefore, undertake our experiment at the Perseus arm segment within $95^\circ \leq l \leq 140^\circ$.

At these longitudes, in the Local Standard of Rest (LSR) frame, the velocity (v_{LSR}) of the Perseus arm material is between -70 to -25 km s^{-1} , which is well-separated from the local gas by ~ 20 – 40 km s^{-1} (Dame et al. 1987; Reid et al. 2009, 2014, 2016). In the extraplanar region, this $[-70, -25]$ km s^{-1} velocity range can be associated with cloud complexes—1) infalling material accreted from the CGM; 2) material in the vertical extension of the arm; 3) galactic fountain material vertically rising from or falling into the arm (Kuntz & Danly 1996; Albert & Danly 2004; Lehner et al. 2022; Marasco et al. 2022). These three types of gas structures at $|v_{\text{LSR}}| \simeq 40$ – 90 km s^{-1} are generally classified as IVCs (Kuntz & Danly 1996; Richter et al. 2001; Lehner et al. 2022) which mostly reside within $|z| \leq 1.5$ kpc (Wakker 2001; Lehner et al. 2022). However, the type 1 IVCs are of external origin; therefore, if present, can contaminate the Perseus absorption. Within our cho-

sen longitude range, the northern infalling IV Arch is one such potential contaminant to the Perseus absorption (Wakker 2001). Moreover, in the second Galactic quadrant, the northern disk is warped just outside the solar circle (Kerr et al. 1957; Oort et al. 1958; Dickey & Lockman 1990), which could also impact the column density measurements. Therefore, we restrict our target search area only to the southern Galactic hemisphere. Figure 12 in Wakker (2001) indicates that the PP Arch could contaminate our column density measurements at $b < -46^\circ$, we further limit the target sample to $-46^\circ < b < 0^\circ$.

Since accurate column density measurements require resolving the Perseus absorption, we only consider targets observed with HST/STIS E140M, E140H, HST/COS G130M, and G160M at spectral resolutions ranging from 2.7 km s^{-1} (STIS E140H) to ~ 20 km s^{-1} (COS) with signal-to-noise $S/N \gtrsim 4$ per pixel. These UV spectrographs cover many species, but in this paper, we only focus on S II, Si IV, and C IV absorption lines. We retrieved the archival spectra of the required quality for AGNs and OB-type stars within the selected longitude and latitude ranges.¹ We use only OB-type stars since their stellar winds typically produce well-defined P-Cygni profiles in the high ions, ensuring that the continuum placement near the absorption lines (e.g., C IV and Si IV) can be reliably modeled (e.g., Bowen et al. 2008; Lehner et al. 2011). Their high rotation velocities also lead to broader stellar lines compared to the ISM ones, minimizing the chance of stellar photospheric features contaminating the ISM lines.

Although AGNs have cosmological distances readily placing them behind the Perseus arm, stellar distances must exceed the estimated distance of the Perseus arm in their directions. We verify this using the accurate stellar distances obtained from Gaia parallaxes (Lindgren et al. 2021). With the release of Gaia EDR3, the reliability of parallax-based distances has improved. For stars within a few kpc of the sun, the typical parallax errors are $\sigma_\varpi/\varpi < 25\%$, ensuring reliable distance measurements. Using their log periodic spiral equation and the associated Perseus arm parameters from Table 2 in Reid et al. (2014), we derive its longitude-dependent mid-arm distances and identify 6 OB-type stars, all $\geq 1\sigma$ behind the Perseus arm.

Figure 2 shows our sample sightline locations with respect to the Sun. The upper panel shows the projected out-of-plane positions, and the lower panel displays the

¹ Though 4 stars in our sample have the FUSE Galactic O VI data, none of the AGN sightlines do. We, therefore, do not include the O VI data in our analysis.

projected in-plane positions of the sightlines and the spiral arms. Our sightlines are evenly distributed over a small segment of the Perseus arm within $95^\circ < l < 140^\circ$ and passing underneath at $0.07 < |z_P| < 3.3$ kpc. In order of increasing $|z_P|$, Table 1 presents the target name (Column 1), target ID (Column 2), Galactic coordinates (Columns 3,4), spectral type (Column 5), parallax-based distances to the targets (Column 6), distances to the Perseus arm from Reid et al. (2014) (Column 7), sightlines’ mid-arm heights, $|z_P|$ (Column 8), instruments used for target acquisition (Column 9), Si IV and C IV S/N (Column 10).

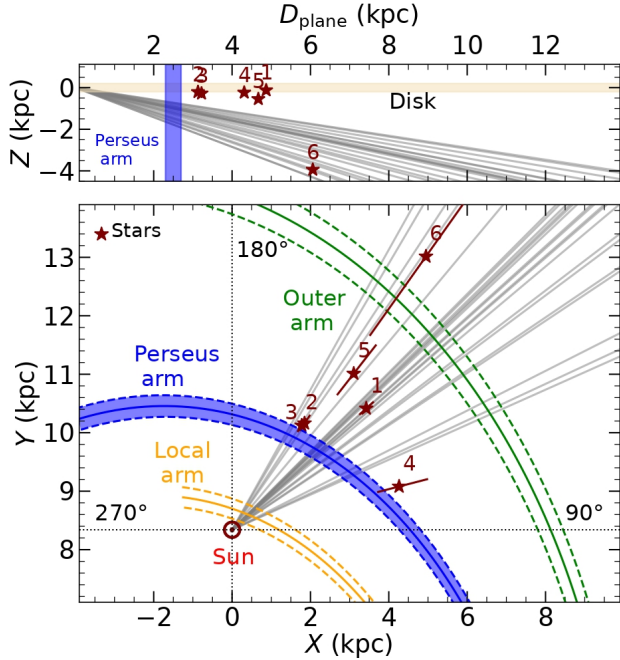


Figure 2. The projected locations of our sightlines through the outer Galaxy. The top panel displays the z -projection of the sightlines as a function of radial distance on the Galactic plane, D_{plane} , from the Sun. The thin disk, indicated by the yellow region, has a 200–300 pc scale height. Each sightline passes below the ~ 400 pc wide Perseus arm (vertical blue region, Reid et al. 2014) at mid-arm height $|z_P|$ (see Table 1 Column 8). The bottom panel shows the projected in-plane positions of the Local, Perseus, and Outer spiral arms (Reid et al. 2014), along with our stellar and AGN sightlines that are distributed evenly over $95^\circ < l < 145^\circ$ and projected behind the Perseus arm.

4. DATA ORIGINS AND ANALYSIS

In this work, we analyze the ISM $\lambda\lambda 1250$, 1253 lines of the S II triplet ($\lambda 1259$ line is heavily saturated and blended with the Si II $\lambda 1260$ line), Si IV doublet lines ($\lambda\lambda 1393$, 1402), and C IV doublet lines ($\lambda\lambda 1548$, 1550), toward the sample stars and AGNs observed with STIS

and COS spectrographs (see below). We also use the Galactic H I 21-cm emission data in the directions of our targets from the Effelsberg-Bonn H I Survey (EBHIS, Winkel et al. 2010). The H I and S II data help, in particular, constrain the Perseus velocity range (see Section 4.5). We summarize the data acquisition and reduction below.

4.1. STIS Echelle Data

The STIS FUV MAMA detectors took the stellar spectra in photon accumulation mode using E140H and E140M echelle gratings. Four stars (PG0122+214, HD 14434, HD 13745, BD+60 73) were observed through the $0''.2 \times 0''.2$ aperture with E140M grating, covering between 1144–1729 Å, observing all three ions. HD 232522 was observed through the $0''.2 \times 0''.2$ aperture with E140H grating between 1140–1517 Å, thus lacking C IV coverage. For HD 210809, the $0''.2 \times 0''.09$ aperture with E140H grating covered S II and the $0''.2 \times 0''.2$ aperture with E140M grating covered the high ions.

The STIS spectral resolution ranges from $R \equiv \lambda/\Delta\lambda = 114,000$ ($\Delta v = 2.7 \text{ km s}^{-1}$) with E140H to 45,800 ($\Delta v = 6.5 \text{ km s}^{-1}$) with E140M. Details on STIS instrumentation can be found in Woodgate et al. (1998) and Branton & Riley (2021). Kimble et al. (1998) summarize its on-orbit performance. We retrieved the reduced 1D spectra (Pipeline CALSTIS 3.4.2) from MAST. Since the CALSTIS pipeline does not coadd exposures, we used our coaddition software to produce a weighted coadded spectrum of all exposures for each target. The final coadded spectra have the heliocentric wavelength scale shifted to the LSR frame.

4.2. COS Data

All the AGNs in our sample are from Project AMIGA (Lehner et al. 2020), and we adopted their reduced coadded COS G130M and G160M spectra, providing a continuous wavelength coverage between 1140–1770 Å. We refer the reader to Section 2 in Lehner et al. (2020) for more detail on the alignment and coaddition procedures of these data. The important outcome from their careful alignments is that the absolute COS velocity calibration is accurate to better than a few km s^{-1} .

4.3. H I 21-cm Data

We use H I 21-cm emission data of the sky toward each target from the EBHIS survey (Winkel et al. 2010). The H I 21-cm emission in these directions has been mapped with the Effelsberg 100-meter Radio Telescope at angular resolution $\sim 10''.8$ and velocity resolution $\Delta v \sim 1.44 \text{ km s}^{-1}$. The high angular resolution of the EBHIS data is advantageous for comparing the H I 21-cm profiles

against the STIS S II spectra. However, some of the kinematic differences between the UV absorption and H I emission data occur owing to comparing essentially a pencil-beam sightline to a $\sim 10.8'$ pointing and the H I emission arising both in the foreground and background of the stars. The EBHIS data reduction pipeline applies stray radiation correction, RFI subtraction, baseline correction, flux, and wavelength calibration. Details of the reduction process and data products can be found in Winkel et al. (2010).

4.4. Continuum Normalization and Column Density Profiles

To analyze the STIS and COS data, first, we model the continuum roughly over $100\text{--}1000\text{ km s}^{-1}$ on either side of the ISM line using a Legendre polynomial. The exact velocity range and polynomial order depend on the line complexity and continuum properties. AGN continua are usually fitted with a 1st or 2nd-order polynomial. However, stellar continua are more complex due to complicated stellar wind profiles and photospheric lines, requiring a 1st to 5th-order fit. The continuum normalized flux is defined as $F_n(v) = F_o(v)/F_c(v)$, where $F_o(v)$ is the observed flux and $F_c(v)$ is the continuum model. We then convert $F_n(v)$ to apparent optical depth $\tau_a(v) = -\ln[F_n(v)]$ and derive the apparent column density $N_a(v)$ using $N_a(v) = 3.768 \times 10^{14} \tau_a(v)/(f\lambda)\text{ cm}^{-2}(\text{km s}^{-1})^{-1}$ (Savage & Sembach 1991), where f is the oscillator strength and λ is the wavelength in Å.

Figure 3 shows an example—the raw flux with the continuum fits (left panels) and normalized flux (middle panels) of the S II $\lambda\lambda 1250, 1253$ transitions, Si IV, and C IV doublets toward BD+60 73. The other sightlines are presented in the Appendix A. As we see, the continua around all the ISM lines toward BD+60 73 are straightforward. However, for two stars, owing to the unreliable continuum model, we could use only one of the Si IV transitions— $\lambda 1402$ line toward HD 210809 and Si IV $\lambda 1393$ toward HD 13745.

In the right panel of Figure 3, we show the H I 21-cm brightness temperature profile, $T_b(v)$ (K), in the direction of BD+60 73 at the top, followed by the $N_a(v)$ profiles of S II, Si IV, C IV lines. This aids in understanding the evolution of the emission/absorption line profiles with changing ionization energy, thus confidently identifying the Perseus velocity range in each ion and H I (see Section 4.5).

In each bottom right panel, overplotting an ion's $N_a(v)$ profiles of two transitions with different strengths ($f\lambda$) also helps diagnose any potential contamination or saturation issues. The former may affect any part of a line, while saturation predominantly affects the line

core. Section 4.6 describes our saturation treatment. Toward our stars, the ISM lines are free of contamination from circumstellar gas, wind, or photospheric absorption. In the case of the AGNs, higher redshift absorbers can contaminate the ISM absorption, as evident in several cases. We removed the following contaminated transitions from our sample: Si IV $\lambda 1402$ toward PG0003+158, S II $\lambda 1250$ and C IV $\lambda 1548$ toward 4C25.01, C IV $\lambda 1550$ toward MRK335 and 3C66A, and S II $\lambda 1250$ toward Zw535.012.

4.5. The Perseus Velocity Range

To delineate the velocity range associated with Perseus absorption/emission, we first inspect the H I and S II profiles, which have narrower and better-defined components than the high ions. However, the larger beam size and broader intrinsic line width of H I, as well as S II arising in the ionized (rather than neutral) regions of the gas, may lead to slight differences between H I and S II velocity ranges. Additionally, H I may include emission from the material behind the stars and Perseus arm. We, therefore, first define the Perseus velocity range using S II and cross-check it against H I before assessing C IV and Si IV.

Visually, two major components are identifiable in S II and H I: one component centered at $v \sim 0\text{ km s}^{-1}$ associated with the local gas, and the other component centered at $-45 \pm 5\text{ km s}^{-1}$ associated with the Perseus arm. The high ion Perseus absorption may be at more negative velocities, e.g., shifted by -15 to -20 km s^{-1} relative to S II and H I toward HD 14434 and HD 13745.

When Perseus and local gas are resolved in S II, we define v_2 , Perseus velocity upper bound, at the shoulder between components where the $N_a(v)$ profile intensity drops significantly. The adopted S II v_2 generally agrees with H I; where discrepant, we define H I v_2 separately using the same approach. For the blended components, clues from both S II and H I set $v_2 \approx -25 \pm 10\text{ km s}^{-1}$. When local and Perseus absorption components are resolved in the high ion profiles, we use the same technique to define v_2 in Si IV and C IV; otherwise, we adopt v_2 from S II. We choose a nominal spread of $2\text{--}5\text{ km s}^{-1}$ about v_2 to account for the systematic uncertainties associated with separating Perseus and local gas in each ion.

Careful attention sets v_1 , the Perseus velocity lower bound, since H I and AGN sightlines may show absorption from the material behind the Perseus arm at $v_{\text{LSR}} < -90\text{ km s}^{-1}$. However, no sightline shows S II absorption at $v_{\text{LSR}} < -90\text{ km s}^{-1}$. S II v_1 is set where the $N_a(v)$ profile first drops to zero (usually $-90 < v_1 < -50\text{ km s}^{-1}$) and is adopted for the other ions and H I. Ex-

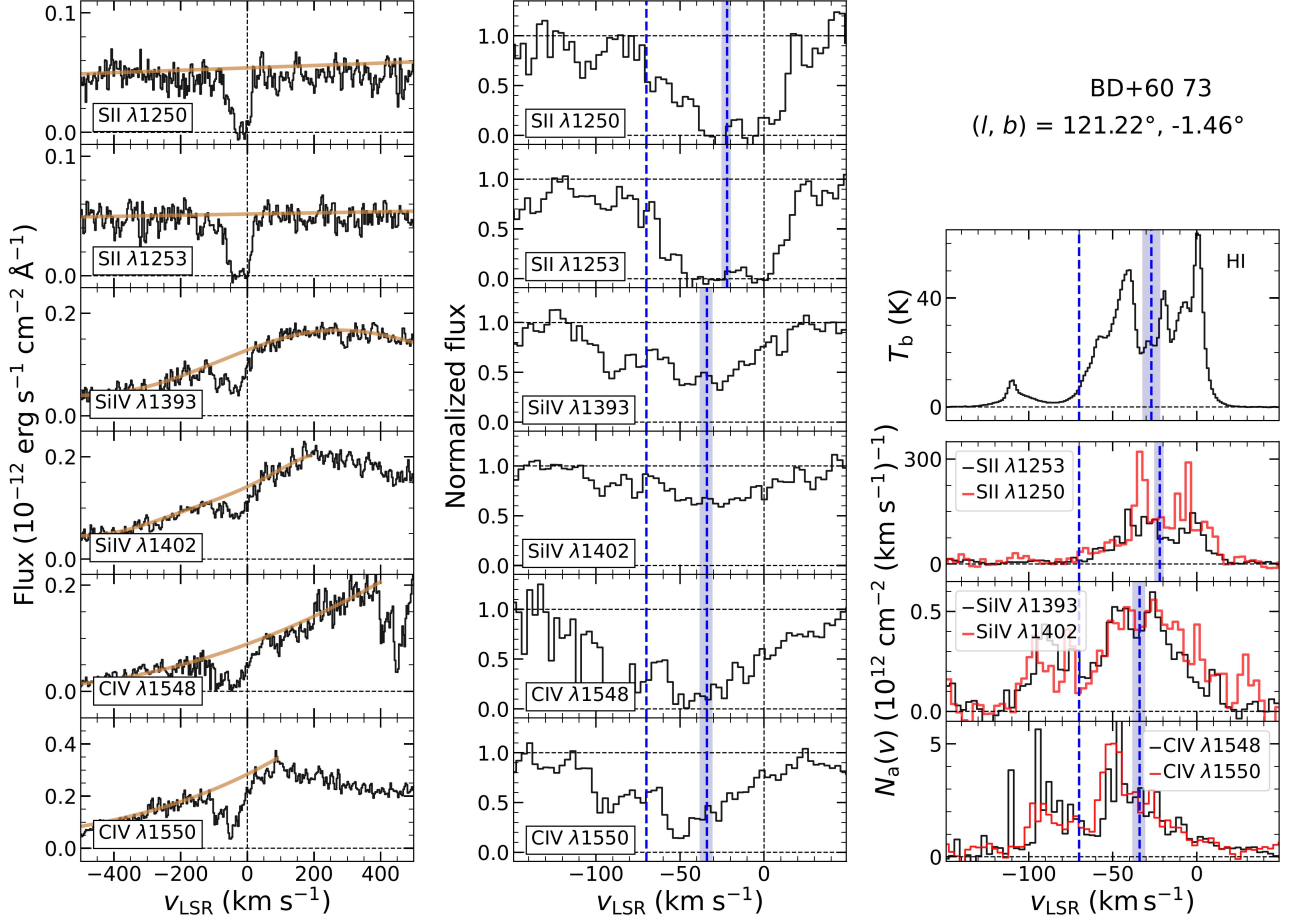


Figure 3. *Left:* the observed flux and continuum models (solid golden lines) and *middle:* normalized flux of S II ($\lambda\lambda 1250, 1253$), Si IV ($\lambda\lambda 1393, 1402$), and C IV ($\lambda\lambda 1548, 1550$) against the LSR velocity toward BD+60 73. *Right:* the H I 21-cm brightness temperature profile, $T_b(v)$, and apparent column density, $N_a(v)$, profiles derived from the normalized flux of S II, Si IV, and C IV transitions. In the left and middle panels, we mark the absorption from the local gas centered at $v = 0 \text{ km s}^{-1}$ by the black-dash line. In the middle and right panels, the blue-dash lines indicate the velocity range $[v_1, v_2]$ of the absorption from the Perseus arm material, and the blue shaded region around v_2 indicates the corresponding systematic uncertainty (see Section 4.5 for more details). The other sightlines are presented in the Appendix.

ceptions are the HD 14434, HD 13745, and HD 232522 sightlines where high and low ions' velocity ranges are very different, and toward HD 210809, high ion absorption lines are broader than S II and H I. Thus, in these sightlines, high ion v_1 is more negative than that of S II (still $\geq -100 \text{ km s}^{-1}$).

Figure 3 shows the adopted Perseus velocity ranges $[v_1, v_2]$ and the systematic uncertainties on v_2 (the blue-dash lines and the blue shaded region in the middle and right panels) toward BD+60 73. Here, the same v_1 is adopted for all the ions and H I. The Perseus and local absorption components are resolved in H I, S II, and Si IV, and thus, their v_2 are set at the trough between the Perseus and local absorption. For C IV, we adopt Si IV v_2 . In this direction, the high ion v_2 is 12 km s^{-1} lower than the S II v_2 . Table 2 compiles the adopted

$[v_1, v_2]$ and systematic uncertainties on v_2 in each ion along each direction.

4.6. The Total Apparent Column Density of Perseus Gas

For each ion, we derive the total apparent Perseus column density, N_a , of each transition by integrating its $N_a(v)$ profile over the Perseus velocities $[v_1, v_2]$, e.g., $N_a = \int_{v_1}^{v_2} N_a(v) dv$ (Savage & Sembach 1991). We report the weighted average as the adopted Perseus column density, $N(z_p)$, of an ion when its two transitions are unsaturated such that the apparent column densities, N_a , estimated for the two transitions of the ion agree within 1σ . All Si IV and C IV doublets in our sample are

Table 2. Perseus Velocity Integration Ranges, $[v_1, v_2]$.

Targets	H I	S II	C IV	Si IV
	(km s ⁻¹)	(km s ⁻¹)	(km s ⁻¹)	(km s ⁻¹)
BD+60 73	[-70, -27 ± 5]	[-70, -22 (⁺² ₋₃)]	[-70, -34 (⁺³ ₋₄)]	[-70, -34 (⁺³ ₋₄)]
HD 14434	[-73, -22 ± 2]	[-73, -32 ± 2]	[-100, -30 ± 5]	[-100, -30 ± 5]
HD 210809	[-50, -20 ± 5]	[-50, -20 ± 5]	[-70, -18 ± -3]	[-70, -18 ± -3]
HD 13745	[-85, -25 (⁺⁴ ₋₄)]	[-85, -25 (⁺² ₋₄)]	[-100, -25 (⁺³ ₋₂)]	[-100, -25 (⁺³ ₋₂)]
HD 232522	[-70, -26 ± 2]	[-70, -26 ± 2]	...	[-90, -35 ± 3]
3C66A	[-80, -20 ± 5]	[-80, -20 ± 5]	[-80, -20 ± 5]	[-80, -20 ± 5]
Zw535.012	[-80, -42 (⁺⁴ ₋₃)]	[-80, -35 ± 5]	[-80, -35 ± 5]	[-80, -35 ± 5]
FBS0150+396	[-70, -18 (⁺³ ₋₄)]	[-70, -18 (⁺³ ₋₄)]	[-70, -18 (⁺³ ₋₄)]	[-70, -18 ± 3]
IRASF00040+4325	[-80, -20 ± 1]	[-80, -20 ± 1]	[-80, -20 ± 1]	[-80, -20 ± 1]
UVQSJ001903.85+423809.0	[-80, -24 ± 2]	[-75, -24 ± 2]	[-75, -24 ± 2]	[-75, -24 ± 2]
PGC2304	[-75, -25 ± 5]	[-75, -25 ± 2]	[-75, -25 ± 2]	[-75, -25 ± 2]
RXSJ0118.8+3836	[-80, -15 ± 1]	[-80, -15 ± 1]	[-80, -15 ± 1]	[-80, -15 ± 1]
IVZw29	[-80, -20 ± 2]	[-80, -20 ± 2]	[-80, -20 ± 2]	[-80, -20 ± 2]
RXJ0049.8+3931	[-75, -20 (⁺⁵ ₋₃)]	[-75, -20 (⁺⁵ ₋₃)]	[-75, -20 (⁺⁵ ₋₃)]	[-75, -20 ± 5]
RXJ0048.3+3941	[-75, -20 ± 1]	[-75, -20 ± 1]	[-75, -20 ± 1]	[-75, -20 ± 1]
LAMOSTJ003432.52+391836.1	[-75, -25 ± 2]	[-75, -25 ± 2]	[-75, -25 ± 2]	[-75, -25 ± 2]
RXSJ0155.6+3115	[-70, -25 (⁺³ ₋₅)]	[-70, -20 ± 1]	[-70, -20 ± 1]	[-70, -20 ± 1]
RXJ0043.6+3725	[-70, -20 (⁺⁴ ₋₅)]	[-70, -20 ± 1]	[-70, -20 ± 1]	[-70, -20 ± 1]
3C48.0	[-75, -27 (⁺² ₋₃)]	[-75, -27 (⁺² ₋₃)]	[-75, -27 (⁺² ₋₃)]	[-75, -27 ± 2]
RXJ0050.8+3536	[-75, -20 ± 5]	[-75, -20 ± 1]	[-75, -20 ± 1]	[-75, -20 ± 1]
RXJ0028.1+3103	[-75, -32 (⁺² ₋₃)]	[-75, -25 ± 5]	[-75, -25 ± 5]	[-75, -25 ± 5]
PG0052+251	[-66, -20 (⁺¹ ₋₂)]	[-66, -20 (⁺¹ ₋₂)]	[-66, -20 (⁺¹ ₋₂)]	[-66, -20 ± 1]
PG0122+214	[-70, -20 (⁺¹ ₋₃)]	[-70, -20 (⁺¹ ₋₃)]	[-70, -20 (⁺⁵ ₋₅)]	[-80, -20 ± 5]
4C25.01	[-70, -20 (⁺¹ ₋₄)]	[-70, -20 (⁺¹ ₋₄)]	[-75, -20 (⁺¹ ₋₄)]	[-70, -20 ± 1]
RXJ0053.7+2232	[-75, -20 ± 1]	[-75, -20 ± 1]	[-75, -20 ± 1]	[-75, -20 ± 1]
RBS2055	[-70, -22 ± 2]	[-70, -22 ± 2]	[-70, -22 ± 2]	[-70, -22 ± 2]
MRK1148	[-65, -21 (⁺¹ ₋₄)]	[-65, -25 ± 5]	[-75, -25 ± 5]	[-65, -25 ± 5]
MRK335	[-90, -21 (⁺² ₋₃)]	[-90, -30 ± 2]	[-90, -30 ± 2]	[-90, -30 ± 2]
PG0003+158	[-70, -22 (⁺² ₋₃)]	[-70, -25 ± 5]	[-70, -25 ± 5]	[-70, -25 ± 5]

NOTE— The errors represent the systematic uncertainties on v_2 .

unsaturated, but there are one Si IV and two C IV non-detections, for which upper limits are estimated at the $< 3\sigma$ level. For H I, we report the adopted Perseus column density, $N(z_P) = N_a = 1.8 \times 10^{18} \text{ cm}^{-2} \int_{v_1}^{v_2} T_b(v) dv$, where $T_b(v)$ (in K) is the H I 21 cm brightness temperature profile.

In S II, when there is evidence of saturation and $\Delta \log N_a$ (the difference between the weak and strong line column densities) of the two S II lines is ≤ 0.12 dex, we apply a saturation correction to the column density following [Savage & Sembach \(1991\)](#) and [Wotta et al. \(2016\)](#). Larger differences indicate saturation is too significant to correct. In that case, we report the S II $\lambda 1253$ line's N_a value as a lower limit on $N(z_P)$.

We also estimate the systematic uncertainty in N_a caused by the possible variations in the velocity range

used for integrating the $N_a(v)$ profiles—related to the systematic uncertainty on v_2 (see Section 4.5). Table 3 presents the adopted column densities, $N(z_P)$, with statistical and systematic uncertainties or lower/upper limits in cases of saturation/non-detection.

5. RESULTS

5.1. Comparison of the $N_a(v)$ Profiles

In Figure 4, we compare the Si IV $N_a(v)$ profiles to the S II profiles. For visual comparison, toward each sightline, we scale the S II profile down by the $\langle \log N_{\text{SiIV}}/N_{\text{SII}} \rangle$ value estimated over the Perseus velocity range along the sightline. We only focus on the Perseus absorption in each profile and find: 1) large scaling factors are needed for S II profiles at all $|z_P|$, indicating that S II profiles are significantly stronger than

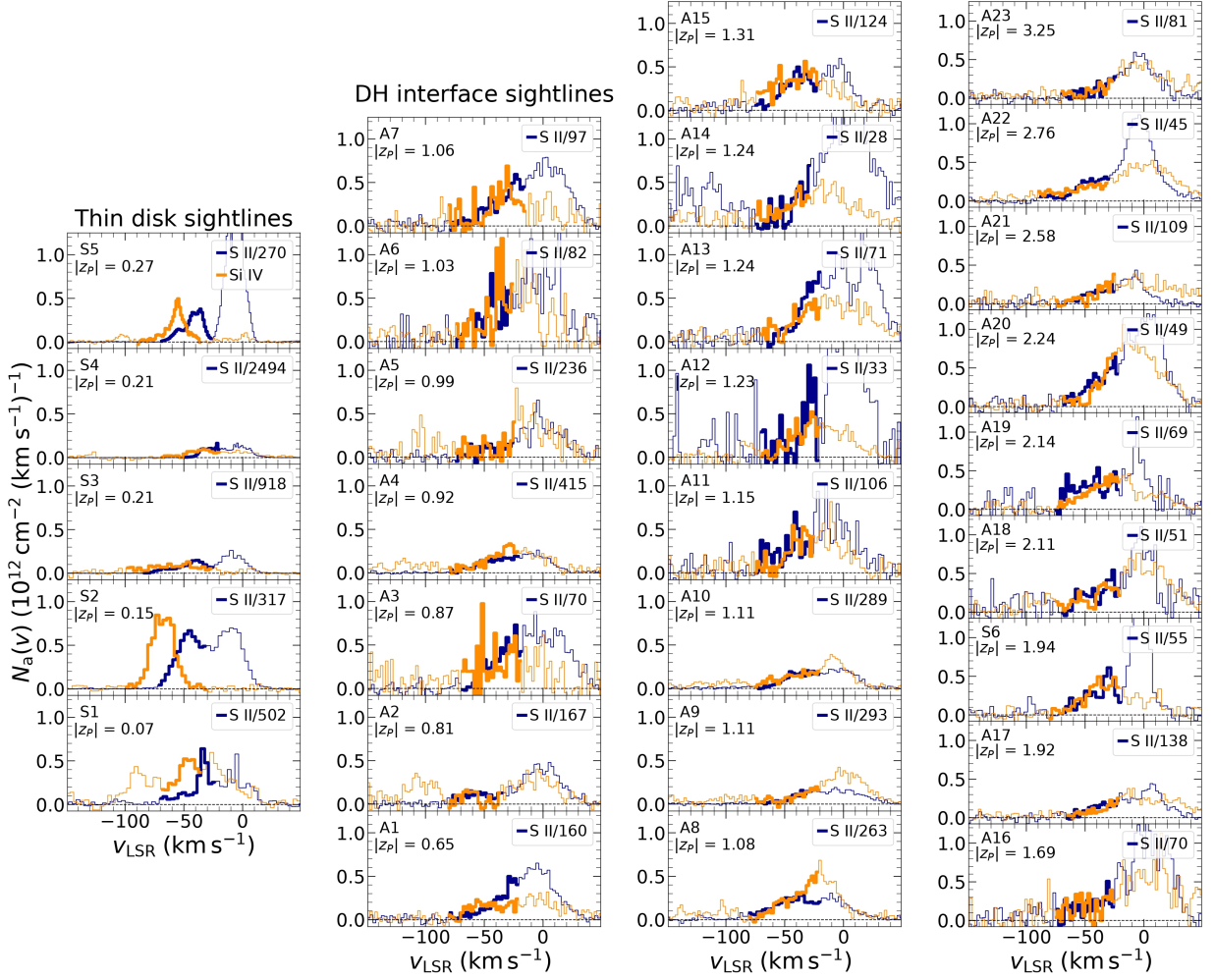


Figure 4. Toward each sightline, we compare the Si IV $N_a(v)$ (orange) profile to the scaled S II profile (blue). The S II scaling factor in each sightline is the average $N_{\text{Si IV}}/N_{\text{S II}}$ value estimated within the Perseus velocity range of that sightline. The sightline ID, mid-arm height $|z_P|$ (kpc) below the Perseus arm are given on the left, and the S II scaling factor is given on the right of each panel. The Perseus absorption toward each sightline in each ion is highlighted with a thicker line. The leftmost panels are thin-disk sightlines at $|z_P| < 0.5$ kpc below Perseus arm, and the rest are the disk-halo interface sightlines at $|z_P| > 0.5$ kpc. The sightlines are stacked from the bottom to the top in ascending mid-arm heights, $|z_P|$.

Si IV; 2) in the thin disk, the scaled S II $N_a(v)$ profiles are usually kinematically very different from the Si IV profiles over the Perseus velocity range; 3) in the disk-halo interface, Si IV and scaled S II $N_a(v)$ profiles kinematically follow each other very well. Additionally, in the thin disk, the Si IV to S II column density ratios vary substantially at different velocities. In the disk-halo interface, column density ratios tend to be very similar at all Perseus velocities toward a given sight line—consequence of good kinematic agreement between the S II and Si IV profiles in the disk-halo interface. The well-matched scaled S II and Si IV $N_a(v)$ profiles in the halo star PG0122+214’s medium-resolution STIS spectra indicates that the agreement in S II and Si IV COS AGN spectra is not an artifact from the coarser COS

resolution. The disk-halo interface sightlines, therefore, suggest a physical relationship between S II and Si IV in the extraplanar Perseus gas, which is not the case for the thin disk sightlines.

In Figure 5, we compare Si IV and C IV $N_a(v)$ profiles. In this case, toward each sightline, the C IV profile is scaled by the $\langle N_{\text{C IV}}/N_{\text{Si IV}} \rangle$ value estimated over Perseus velocities along the sightline. Based on this comparison, we find: 1) C IV is usually 2–4 times stronger than Si IV, except for two thin disk stars, HD 210809 and BD+60 73, where C IV profiles are $> 5\times$ stronger than Si IV; 2) either ion’s $N_a(v)$ profiles are equally strong in the thin disk and the disk-halo interface; and 3) C IV and Si IV $N_a(v)$ profiles closely mirror each other in all the sightlines, indicating these two ions’

kinematic similarities in the thin disk and disk-halo interface. Additionally, the ratio of C IV to Si IV column densities tends to be similar at all Perseus velocities in the thin disk and the disk-halo interface—consequence of the good kinematic agreement between the $N_a(v)$ profiles of these two ions. This suggests that C IV and Si IV are physically correlated both in the thin disk and the disk-halo interface gas sampled by our sightlines. This also suggests co-spatiality between S II and C IV bearing gas only in the disk-halo interface below the Perseus arm (see Appendix B).

5.2. Kinematics of the Disk-Halo Interface Warm-hot Gas

Feedback-driven bulk transportation of matter from the Perseus arm to the disk-halo interface must lead to nonzero vertical motion in addition to galactic rotation. Consequently, the velocity projections in the sightlines through the disk-halo interface may be slightly offset from average thin disk velocities. For example, [Kepner \(1970\)](#) and [Verschuur \(1973\)](#) found that the extraplanar H I emission above Perseus arm splits into inner and outer spiral-like l - v branches, which is explained by [Sofue & Tosa \(1974\)](#) as rising/falling gas motions. Additionally, extraplanar gas may lag behind disk rotation, as seen in external spiral galaxies (e.g., [Gentile et al. 2013](#); [Zschaechner & Rand 2015](#); [Bizyaev et al. 2017](#); [Levy et al. 2019](#)) and in simulations ([Putman et al. 2012](#)). Such rotational lag would also offset disk-halo interface sightlines’ gas velocities. Therefore, we investigate the extraplanar Perseus gas kinematics as a function of galactic longitude (l) and height ($|z_P|$).

Figure 6 shows the l (left) and $|z_P|$ (right) distributions of apparent optical depth weighted average Perseus velocities (v_a) and the velocity ranges containing 90% of Perseus absorption (Δv_{90}) in S II (top panels) and Si IV (bottom panels). We find: 1) S II v_a ranges between -55 km s^{-1} to -25 km s^{-1} with Δv_{90} typically spanning over $[-80, -20] \text{ km s}^{-1}$; 2) except for the sightlines toward HD 14434, HD 13745, and HD 232522, Si IV v_a and Δv_{90} are consistent with S II within $\sim 5 \text{ km s}^{-1}$; 3) both ions’ v_a ’s, with substantial scatter ($\sim 6 \text{ km s}^{-1}$), follow the expected l - v trend for the Perseus arm material (black-dash line in the left panels of Figure 6, [Choi et al. 2014](#))—no bifurcation in v_a about the Perseus track indicating a lack of vertical motion in the extraplanar Perseus gas; and 4) none of the ion’s v_a or Δv_{90} depend on $|z_P|$ —indicating no rotation lag up to 3.3 kpc below Perseus arm. [Savage et al. \(2003\)](#) also reports no

rotation lag in the disk-halo interface gas up to a few kpc.

In conclusion, below the Perseus arm, disk-halo interface gas kinematics purely resemble Galactic rotation. The lack of rising/falling motion in the gas implies limited fountain speed in this region—indicating: 1) feedback is currently quiescent in this region; and 2) any past fountain flow has sufficiently slowed down that its kinematic imprint is small. Our data, particularly in the disk-halo interface sightlines, are unable to capture any vertical motion or rotation lag in the gas.

5.3. Structure of the Extraplanar Warm-Hot Gas

We next examine the extraplanar gas distribution, i.e., the $|z_P|$ -distributions of H I, S II, Si IV, and C IV column densities in Figure 7 (plotted vs. linear $|z_P|$ in the left panel and $\log |z_P|$ in the right panel). We remind readers that the sightlines at $|z_P| < 0.5 \text{ kpc}$ probe the thin disk Perseus arm material, whereas at $|z_P| > 0.5 \text{ kpc}$ probe the disk-halo interface below the Perseus arm. We observe distinct trends in the low and high ions, as discussed below.

In H I we observe: 1) $\log N(z_P)$ sharply drops by ~ 0.8 dex up to $|z_P| \approx 0.5 \text{ kpc}$; 2) at $0.5 < |z_P| < 1.5 \text{ kpc}$, H I $\log N(z_P)$ drops by another ~ 0.5 dex; 3) at $|z_P| > 1.5 \text{ kpc}$, H I $N(z_P)$ does not change at all with increasing $|z_P|$ and has a ~ 0.1 dex scatter. At $|z_P| > 1.5 \text{ kpc}$, we find that H I $\log N(z_P)$ is 0.3–0.5 dex higher than the expectation from a $h_z = 0.5 \text{ kpc}$ exponential scale height (orange solid line in Figure 7; [DL90](#)). This indicates a possibly larger scale height of the H I in the disk-halo interface below the Perseus arm. Within 0.5–3.3 kpc, H I $\log N(z_P)$ drops roughly 1 dex with increasing height—indicating a shallower density distribution in the disk-halo interface than in the thin disk.

S II Perseus absorption is saturated in the thin disk, yet there is a sharp drop in S II $N(z_P)$ with height up to $|z_P| \approx 0.5 \text{ kpc}$. At $0.5 < |z_P| < 1.5 \text{ kpc}$, we see a large scatter (> 1 dex) in $N(z_P)$ with unexpected saturated S II in four sightlines near $|z_P| \sim 1 \text{ kpc}$. We note that the foreground stars with $D_{\text{star}} < 1.5 \text{ kpc}$ from the Sun do not show Perseus-like S II absorption, confirming the saturated absorption arises at $D > 1.5 \text{ kpc}$. These saturated S II lines may be associated with dense structures cooling out of the disk-halo interface gas below the Perseus arm. At $|z_P| > 1.5 \text{ kpc}$, S II $\log N(z_P)$ has a smaller scatter (~ 0.1 dex) and vary little (< 0.1 dex) with increasing $|z_P|$. Again, at $|z_P| > 1.5 \text{ kpc}$, we measure higher S II $N(z_P)$ than expected from the 1 kpc scale height of H α emission probing similar gas phase

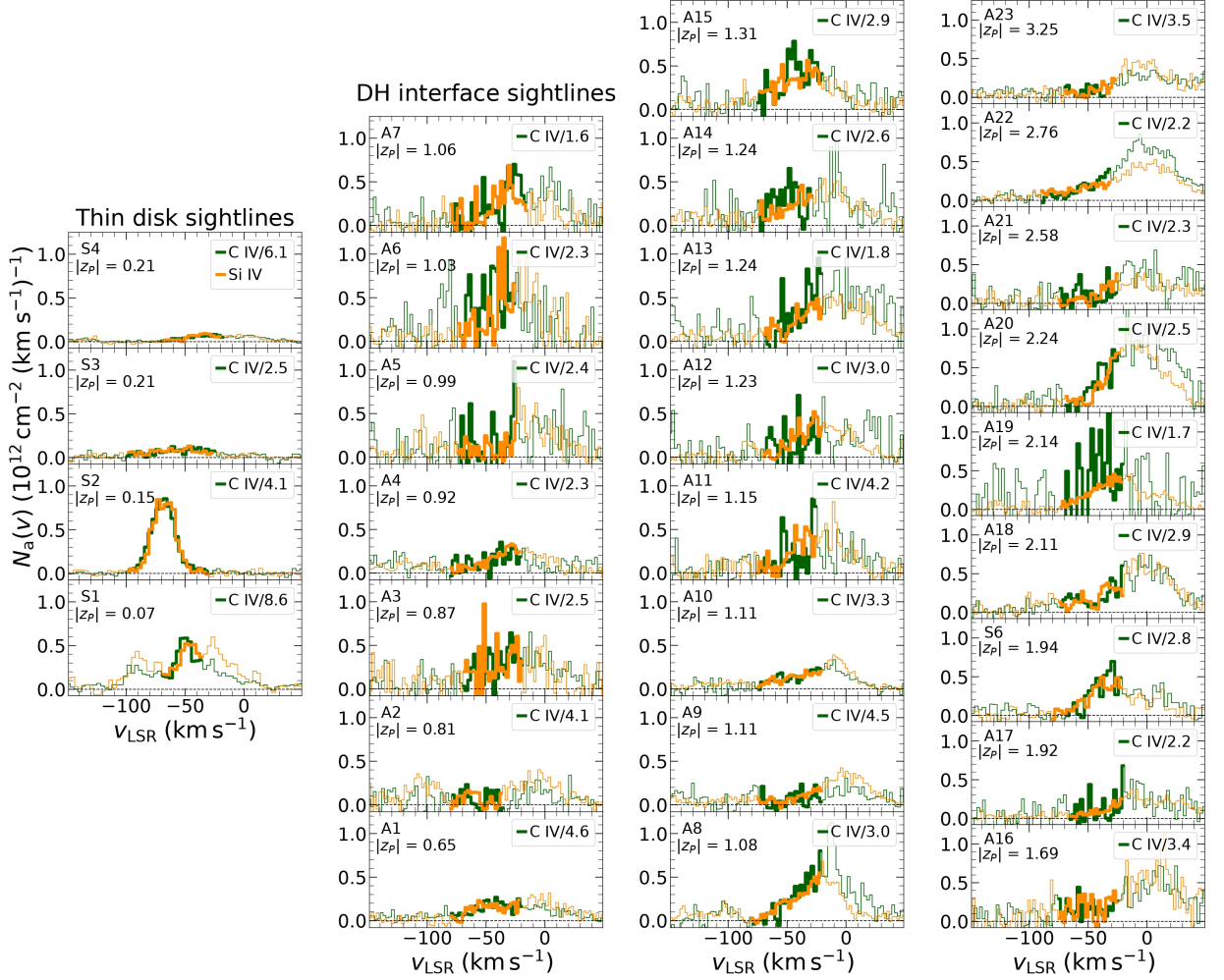


Figure 5. Similar to 4, here we compare the Si IV (orange) $N_a(v)$ profile to the C IV (green) profile, which is scaled down by the average $N_{\text{CIV}}/N_{\text{SiIV}}$ value estimated over the Perseus velocity range of each sightline.

as S II Haffner et al. (1999) (orange solid line in panel 2 Figure 7). Within 0.5–3.3 kpc, the unsaturated S II $\log N(z_p)$ drops only roughly ~ 0.6 dex with increasing height, which is a shallower decline than that in the thin disk.

Unlike the low ions, C IV and Si IV $\log N(z_p)$ exhibit much flatter distributions with similar values and ~ 0.2 dex scatter across the sampled $|z_p|$ range. In the disk-halo interface between $|z_p| = 0.5$ –3.3 kpc, there might be a slight decline (< 0.1 dex) in both high ion column densities with increasing height—possibly comparable to the orange solid lines in the third and fourth panel of Figure 7 showing the Si IV and C IV distributions with 3.2 and 3.6 kpc scale heights from SW09. We remind again that SW09 experiment is different from ours as they measure $N(< z)$.

To test if the $N(z_p)-|z_p|$ distributions are exponential in nature, i.e., $N(z_p) = N_0 \exp[-z_p/h_z]$ with a mid-

plane density N_0 , a scale height h_z , we model the column densities of each ion using a Markov Chain Monte Carlo (MCMC) fitter. We also include an ISM patchiness parameter σ_p to account for the inherent scatter of the gas distribution (SW09). The results are summarized in Table 4. The N_0 and σ_p posterior constraints are well-defined, but none of the h_z is constrained. We, therefore, list the 2σ lower limits (2.5%) of h_z posterior distributions in Table 4, but we caution that these lower limits are prior-dependent. The gray solid line and the gray shaded region in each panel of Figure 7 show the best-fit MCMC model and their 95% CI. As we see, in H I and S II, there is a strong disagreement between our MCMC fits and the flat slab model predictions (orange solid lines). However, despite the poorly constrained scale heights in the high ions, our MCMC fits and the flat slab model predictions do not differ much. This suggests that in the disk-halo interface below the Perseus

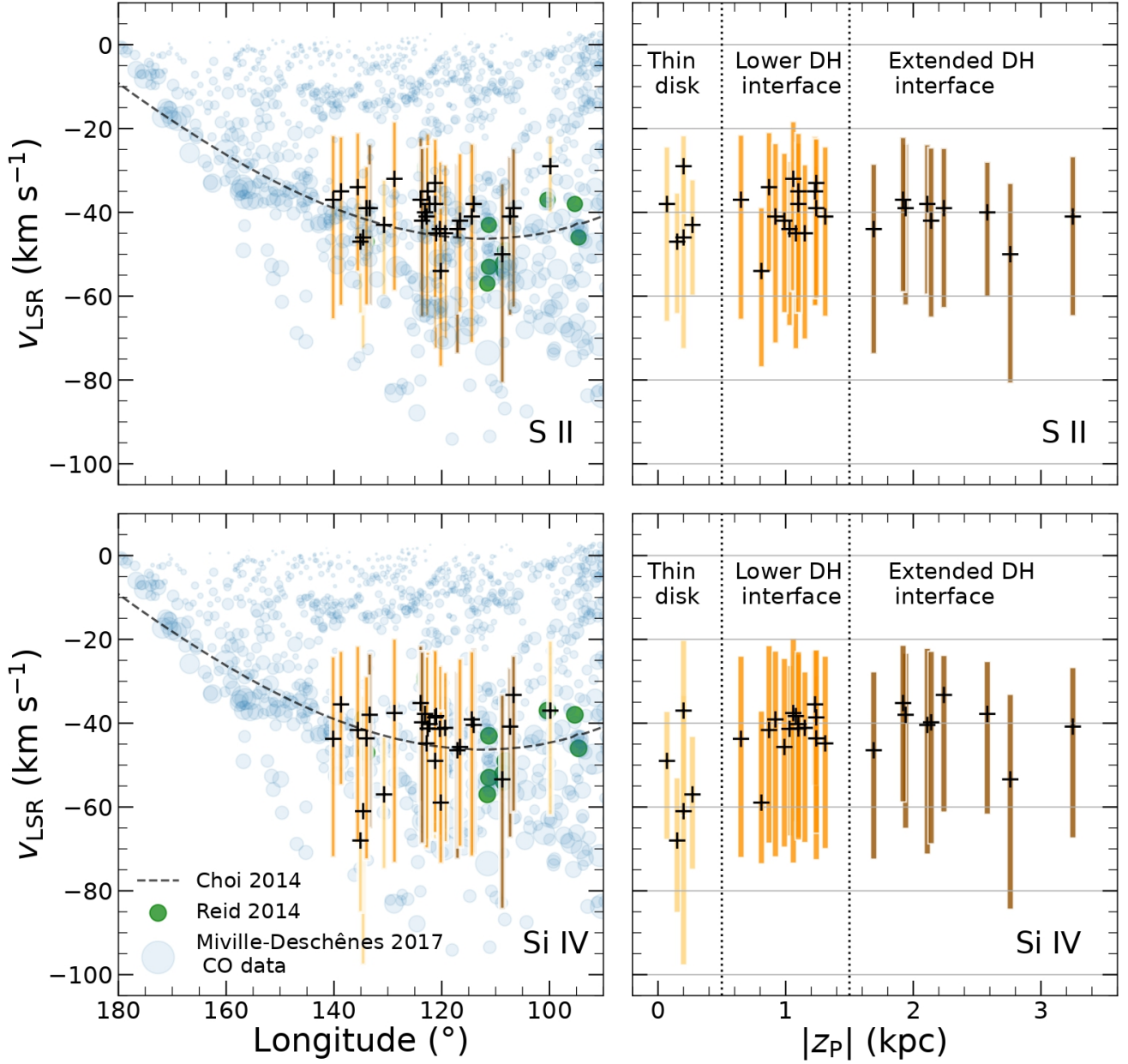


Figure 6. Kinematics of the S II (*top*) and Si IV (*bottom*) absorption associated with the Perseus arm against the Galactic longitude l (*left*) and absolute mid-arm height $|z_{\text{P}}|$ (*right*). The average Perseus velocity, v_a , and the velocity range containing 90% Perseus absorption, Δv_{90} , in S II and Si IV are shown with the plus signs and the vertical bars, respectively. Δv_{90} (the vertical bars) are color-coded based on the mid-arm heights, $|z_{\text{P}}|$, e.g., yellow for $z_{\text{P}} < 0.5$ kpc, orange for $0.5 < z_{\text{P}} < 1.5$ kpc, and brown for $z_{\text{P}} > 1.5$ kpc. The adopted Perseus velocity track from Choi et al. (2014) is shown as a black-dash line in the left panels, along with CO data from Miville-Deschênes et al. (2017) (in light blue circles) and high-mass star-forming region (HMSFR) data from Reid et al. (2014) (in green circles).

Table 3. Adopted Perseus Column Densities.

Target	$\log N_{\text{HI}} (z_P)$ [cm ⁻²]	$\log N_{\text{Si II}} (z_P)$ [cm ⁻²]	$\log N_{\text{Si IV}} (z_P)$ [cm ⁻²]	$\log N_{\text{C IV}} (z_P)$ [cm ⁻²]
BD+60 73	21.321 ± 0.001 (+0.042/-0.034)	> 15.797	13.096 ± 0.022 (+0.041/-0.059)	14.028 ± 0.021 (+0.024/-0.045)
HD 14434	21.225 ± 0.001 (+0.013/-0.007)	> 15.833	13.331 ± 0.010 ± 0.002	13.944 ± 0.006 (+0.003/-0.005)
HD 210809	20.998 ± 0.001 (+0.045/-0.057)	> 15.807	12.410 ± 0.053 ± 0.032	13.194 ± 0.018 (+0.068/-0.041)
HD 13745	21.105 ± 0.001 (+0.016/-0.028)	15.671 ± 0.033	12.708 ± 0.056 (+0.016/-0.009)	13.110 ± 0.055 (+0.032/-0.038)
HD 232522	20.648 ± 0.003 (+0.022/-0.012)	15.278 ± 0.003 (+0.006/-0.005)	12.846 ± 0.018 (+0.001/-0.002)	...
3C66A	20.302 ± 0.008 (+0.103/-0.140)	15.140 ± 0.020 (+0.090/-0.100)	12.935 ± 0.034 (+0.038/-0.048)	13.599 ± 0.037 (+0.037/-0.055)
Zw535.012	19.718 ± 0.023 (+0.047/-0.044)	14.676 ± 0.034 (+0.060/-0.063)	< 12.452	< 13.062
FBS0150+396	20.086 ± 0.012 (+0.048/-0.065)	15.014 ± 0.037 (+0.053/-0.050)	13.163 ± 0.091 (+0.013/-0.025)	13.560 ± 0.040 ± 0.030
IRASF00040+4325	20.300 ± 0.008 (+0.013/-0.015)	> 15.552	12.933 ± 0.028 ± 0.013	13.288 ± 0.053 (+0.012/-0.010)
UVQSJ001903.85+423809.0	20.177 ± 0.011 (+0.023/-0.054)	> 15.080	12.706 ± 0.141 (+0.106/-0.066)	< 13.090
PGC2304	20.113 ± 0.012 (+0.061/-0.071)	15.090 ± 0.050 (+0.020/-0.030)	13.175 ± 0.148 (+0.032/-0.040)	13.540 ± 0.070 ± 0.020
RXSJ0118.8+3836	20.177 ± 0.010 (+0.017/-0.016)	15.110 ± 0.020 ± 0.020	13.121 ± 0.071 (+0.003/-0.006)	13.331 ± 0.094 (+0.012/-0.010)
IVZw29	20.371 ± 0.006 (+0.009/-0.021)	> 15.565	13.145 ± 0.026 (+0.037/-0.039)	13.620 ± 0.020 (+0.030/-0.040)
RXJ0049.8+3931	20.236 ± 0.008 (+0.047/-0.024)	15.123 ± 0.020 (+0.037/-0.079)	12.656 ± 0.042 (+0.100/-0.052)	13.310 ± 0.040 (+0.070/-0.030)
RXJ0048.3+3941	20.212 ± 0.008 (+0.011/-0.012)	15.287 ± 0.027	12.826 ± 0.023 (+0.014/-0.013)	13.350 ± 0.030 ± 0.010
LAMOSTJ003432.52+391836.1	19.998 ± 0.015 ± 0.021	15.060 ± 0.040 ± 0.030	13.031 ± 0.065 (+0.028/-0.032)	13.650 ± 0.090 (+0.030/-0.040)
RXSJ0155.6+3115	19.429 ± 0.044 (+0.066/-0.121)	14.530 ± 0.080 (+0.030/-0.020)	13.003 ± 0.049 (+0.016/-0.015)	13.477 ± 0.078 ± 0.010
RXJ0043.6+3725	20.167 ± 0.010 (+0.028/-0.045)	14.930 ± 0.030 ± 0.020	13.073 ± 0.040 ± 0.015	13.340 ± 0.060 ± 0.020
3C48.0	19.422 ± 0.064 (+0.059/-0.057)	14.436 ± 0.080 (+0.061/-0.110)	12.981 ± 0.046 (+0.030/-0.045)	13.390 ± 0.060 (+0.030/-0.040)
RXJ0050.8+3536	20.110 ± 0.012 (+0.043/-0.047)	> 15.349	13.253 ± 0.031 ± 0.006	13.720 ± 0.030 ± 0.010
RXJ0028.1+3103	19.422 ± 0.048 (+0.021/-0.060)	14.800 ± 0.080 (+0.132/-0.057)	12.950 ± 0.109 (+0.064/-0.085)	13.480 ± 0.040 ± 0.050
PG0052+251	19.601 ± 0.034 (+0.018/-0.040)	14.830 ± 0.020 (+0.020/-0.040)	12.688 ± 0.032 (+0.025/-0.055)	13.041 ± 0.077 (+0.025/-0.046)
PG0122+214	19.464 ± 0.052 (+0.022/-0.039)	14.872 ± 0.021 (+0.008/-0.025)	13.131 ± 0.037 (+0.053/-0.066)	13.573 ± 0.037 (+0.047/-0.070)
4C25.01	19.396 ± 0.054 (+0.024/-0.065)	14.750 ± 0.071 (+0.020/-0.047)	13.035 ± 0.049 (+0.017/-0.051)	13.493 ± 0.052 (+0.025/-0.078)
RXJ0053.7+2232	19.590 ± 0.036 ± 0.013	14.940 ± 0.040 ± 0.010	13.101 ± 0.027 ± 0.013	13.333 ± 0.114 (+0.018/-0.019)
RBS2055	19.681 ± 0.025 (+0.037/-0.018)	14.770 ± 0.020 ± 0.030	13.078 ± 0.041 (+0.052/-0.059)	13.470 ± 0.040 ± 0.050
MRK1148	19.370 ± 0.054 (+0.013/-0.051)	14.740 ± 0.030 (+0.060/-0.090)	12.702 ± 0.073 (+0.093/-0.136)	13.069 ± 0.090 (+0.123/-0.113)
MRK335	19.551 ± 0.046 (+0.028/-0.033)	14.610 ± 0.010 (+0.020/-0.030)	12.949 ± 0.026 (+0.027/-0.026)	13.292 ± 0.036 (+0.027/-0.036)
PG0003+158	19.369 ± 0.063 (+0.068/-0.081)	14.540 ± 0.030 (+0.110/-0.120)	12.627 ± 0.066 (+0.133/-0.140)	13.170 ± 0.040 (+0.090/-0.130)

NOTE—All the column densities are estimated integrating the $N_a(v)$ profiles over the velocity ranges, $[v_1, v_2]$, in Table 2. The first error is the random uncertainty, and the second is the systematic uncertainty associated with isolating Perseus gas from local gas (see Section 4.6 for more details).

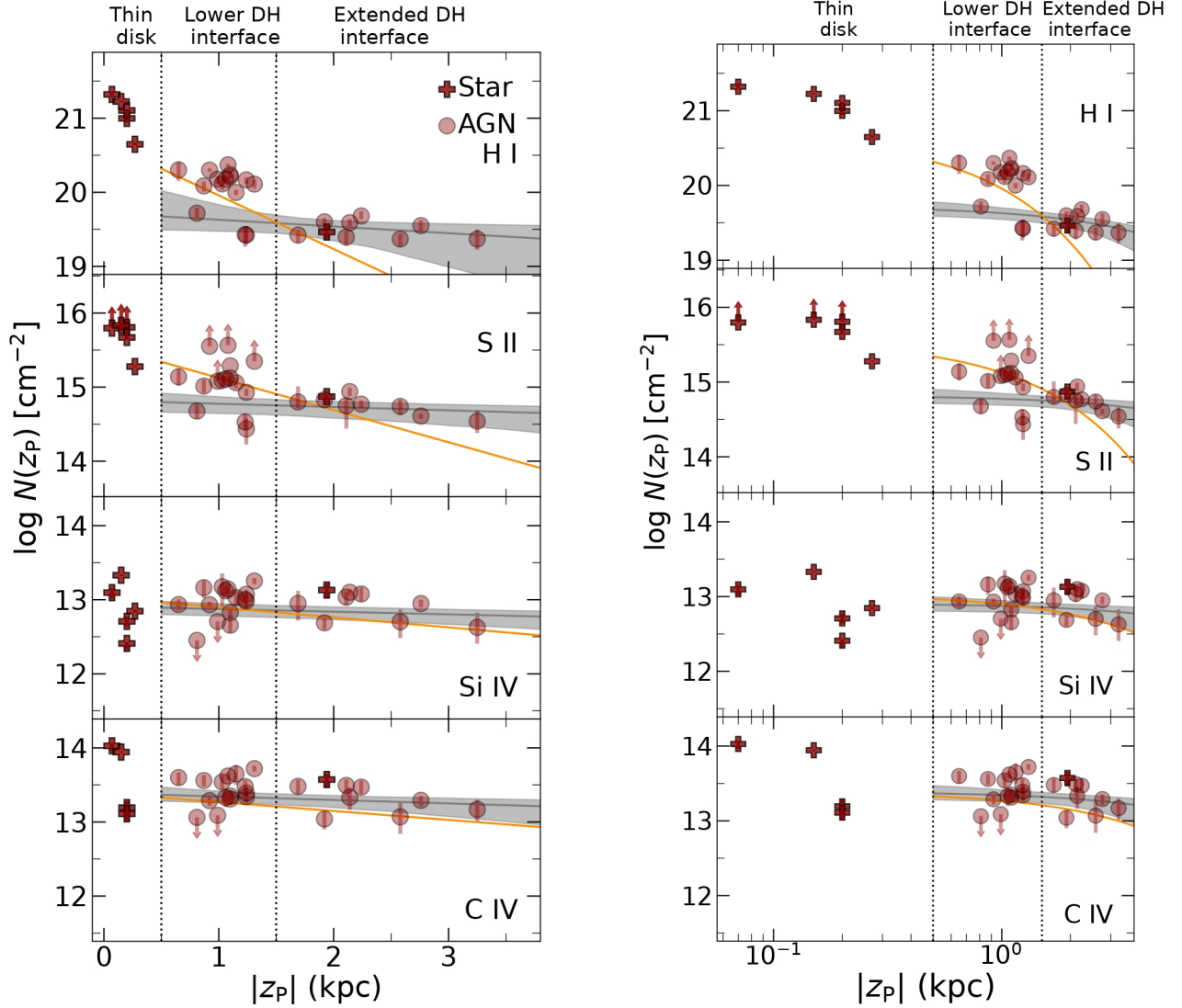


Figure 7. Logarithm of H I, S II, Si IV, and C IV column densities, $N(z_P)$, as a function of $|z_P|$ (*left*) and $\log |z_P|$ (*right*). The dark red pluses and circles are estimated $\log N(z_P)$ in the stellar and AGN sightlines, respectively. The upward and downward arrows indicate lower or upper limits, respectively. The gray solid line in each panel indicates the MCMC best fit to the data at $|z_P| > 0.5$ kpc assuming a single exponential model, and the gray shaded region indicates the 95% confidence interval (CI) of the MCMC fits. The orange solid line indicates the expected column density distribution with exponential scale heights h_z from literature ($h_z = 0.5$ kpc for H I (DL90); 1.0 kpc for H α emission probing similar gas phase as S II (Haffner et al. 1999); 3.2 kpc for C IV, and 3.4 kpc for Si IV, (SW09)).

arm: 1) the neutral/low ionization gas's $N(z_P)$ - $|z_P|$ distribution is more complex than a simple exponential distribution; 2) high ions might follow a simple exponential distribution but with $\gg 3$ kpc scale height.

To summarize, H I and S II have distinct $N(z_P)$ - $|z_P|$ distributions compared to the high ions. Both N_{HI} and N_{SII} sharply decrease with height up to $|z_P| = 1.5$ kpc before flattening out, whereas both high ions' $N(z_P)$ - $|z_P|$ distributions are very flat over the entire $|z_P|$ range probed by our sample. The observed $N(z_P)$ - $|z_P|$ dis-

tributions in the disk-halo interface below the Perseus arm, particularly in the neutral/low ionization gas, are incompatible with the previous exponential scale height characterizations.

5.4. Ion ratios

Using the Perseus column densities in Table 3, we estimate $N_{\text{SiIV}}/N_{\text{SII}}$ and $N_{\text{CIV}}/N_{\text{SiIV}}$. The $N_{\text{SiIV}}/N_{\text{SII}}$ values help determine the dominant phase between the warm and warmer/transition temperature gas (see Sec-

Table 4. MCMC Fit Results of the $N-|z_P|$ Distributions.

Ion	$\log N_0^a$	σ_p^b	h_z^c
	[cm^{-2}]		(kpc)
H I	$19.73^{(+0.34)}_{(-0.13)}$	$0.25^{(+0.04)}_{(-0.04)}$	> 1.26
S II	$14.82^{(+0.10)}_{(-0.07)}$	$0.24^{(+0.06)}_{(-0.04)}$	> 2.86
Si IV	$12.91^{(+0.05)}_{(-0.06)}$	$0.17^{(+0.05)}_{(-0.04)}$	> 4.33
C IV	$13.39^{(+0.05)}_{(-0.09)}$	$0.15^{(+0.04)}_{(-0.03)}$	> 3.02

NOTE—For each ion, we fit a single exponential model to the column density data at $|z_P| \geq 0.5$ kpc. (a): best-fit mid-plane column density with 68% CI, (b): best-fit patchiness parameter with 68% CI, (c): 5th percentiles of H I, S II, Si IV and C IV scale height posterior distributions.

tion 6.3), while $N_{\text{C IV}}/N_{\text{Si IV}}$ is useful to constrain the ionization mechanisms of the highly ionized gas. The change in the ionization conditions in the extraplanar Perseus arm gas can be assessed from the $|z_P|$ -distributions of these ratios.

5.4.1. $N_{\text{Si IV}}/N_{\text{S II}}$ vs $|z_P|$

Figure 8 shows the $|z_P|$ -distribution of $N_{\text{Si IV}}/N_{\text{S II}}$. At $|z_P| < 0.5$ kpc, S II is mostly saturated (3 out of 5 measurements, see panel 2 Figure 7), resulting in $N_{\text{Si IV}}/N_{\text{S II}}$ upper limits at those heights. At $0.5 < |z_P| < 1.5$ kpc, $N_{\text{Si IV}}/N_{\text{S II}}$ gradually increases and plateaus at $|z_P| > 1.5$ kpc with $\langle \log N_{\text{Si IV}}/N_{\text{S II}} \rangle = -1.8 \pm 0.2$. The rise in $N_{\text{Si IV}}/N_{\text{S II}}$ up to 1.5 kpc is primarily due to the large drop in $N_{\text{S II}}$ with increasing $|z_P|$ and $N_{\text{Si IV}}$ barely changing with $|z_P|$ (see Figure 7 panels 2 and 3). At $|z_P| > 1.5$ kpc, $N_{\text{Si IV}}/N_{\text{S II}}$ plateaus owing to the flattened $N_{\text{S II}}$ and $N_{\text{Si IV}}$ distributions at large heights (see section 5.3).

Notably, $N_{\text{Si IV}}/N_{\text{S II}}$ is $\ll 1$ at all $|z_P|$, indicating significantly larger S II column density compared to Si IV as well as C IV (as discussed in section 5.4.2). At $|z_P| > 1.5$ kpc, e.g., in the extended disk-halo interface, the S II column density on average is roughly 60 times higher than Si IV. Previously, using individual sightlines toward inner and outer Galaxy disk and halo stars at $|z_{\text{star}}|$ ranging between 43 pc to 3 kpc, where path length through the thin disk gas dominates, $\log N_{\text{Si IV}}/N_{\text{S II}}$ is found to be between -2.6 to -1.7 dex with no obvious dependence on $|z_{\text{star}}|$ (Spitzer & Fitzpatrick 1992, 1993; Fitzpatrick & Spitzer 1994, 1997; Howk et al. 1999; Brandt et al. 1999; Sembach & Savage 1994; Sembach et al. 1995). Toward globular cluster stars at $|z_{\text{star}}| = 5.3$ and 10 kpc, where path length through the disk-halo interface gas dominates, Howk & Consiglio (2012) found $\log N_{\text{Si IV}}/N_{\text{S II}} = -1.7 \pm 0.02$, and -1.48 ± 0.03 respectively. These Galactic disk and

disk-halo interface $N_{\text{Si IV}}/N_{\text{S II}}$ measurements are fully consistent with our $N_{\text{Si IV}}/N_{\text{S II}}$ values measured below the Perseus arm. Additionally, our and old estimates indicate that $N_{\text{Si IV}}/N_{\text{S II}}$ in the disk-halo interface increases with the increasing height above the plane, but $\ll 1$ —implying that S II column densities are significantly higher than the high ions. Howk & Consiglio (2012) also showed the disk-halo interface gas in their surveyed directions up to 10 kpc above the Galactic plane is predominantly WNM+WIM—given our observed $N_{\text{Si IV}}/N_{\text{S II}}$ values, this might as well be true for the southern vertical extension of the Perseus arm sampled by our sightlines (also see the discussion in Section 6.3). However, it is important to note that we have no information about a hot phase with $T \gtrsim 10^6$ K. X-ray spectroscopy of O VII absorption has indicated that it can be strong in the thin disk and disk-halo regions of the Milky Way (Yao & Wang 2005), and this could be a comparably important phase.

5.4.2. $N_{\text{C IV}}/N_{\text{Si IV}}$ vs $|z_P|$

Figure 9 illustrates the $|z_P|$ -distribution of $N_{\text{C IV}}/N_{\text{Si IV}}$, revealing a notable pattern: the scatter in $N_{\text{C IV}}/N_{\text{Si IV}}$ is smaller in the disk-halo interface gas compared to the thin disk. Strikingly, 21 out of 27 $N_{\text{C IV}}/N_{\text{Si IV}}$ measurements across both thin disk and disk-halo interface sightlines align with the average $\langle N_{\text{C IV}}/N_{\text{Si IV}} \rangle = 2.5 \pm 0.5$, observed in the extended disk-halo interface at $1.5 < |z_P| < 3.3$ kpc.

Six measurements, at $|z_P| < 1.5$ kpc, are more than 1σ higher than this average. Excluding the outlier toward BD+60 73, which is unusually high, the remaining five measurements elevate the ratio to $\langle N_{\text{C IV}}/N_{\text{Si IV}} \rangle = 3.44 \pm 1.36$ at $|z_P| < 1.5$ kpc, which is higher than the disk-halo interface average with a larger scatter. This average is, however, consistent with previous works: $\langle N_{\text{C IV}}/N_{\text{Si IV}} \rangle = 3.3 \pm 2.5$ in the thin disk (Lehner et al.

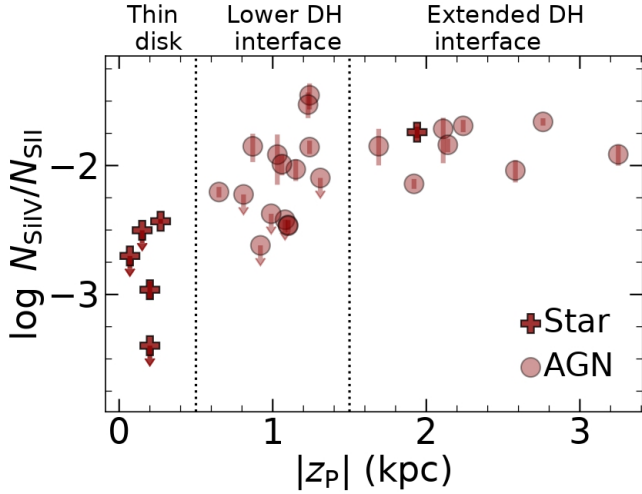


Figure 8. The $|z_P|$ -distribution of $\log N_{\text{SiIV}}/N_{\text{SiII}}$. Symbols are the same as in Figure 7. The data points with downward arrows indicate the upper limits of the ratio due to saturated S II.

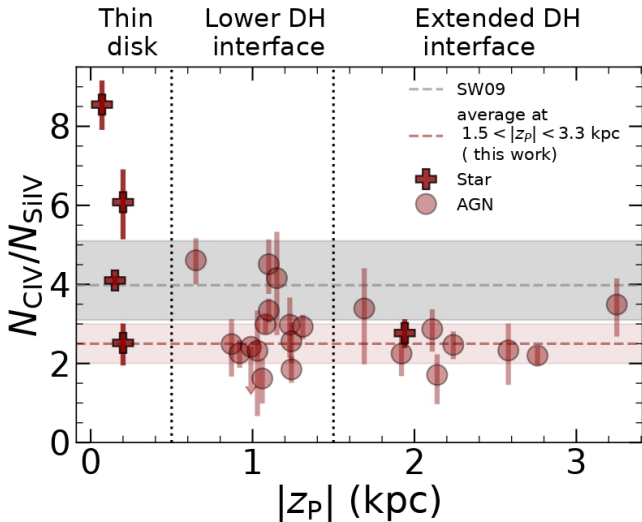


Figure 9. The $|z_P|$ -distribution of $N_{\text{CIV}}/N_{\text{SiIV}}$. Symbols are the same as Figure 7. The gray-dash line is the Galactic average $\langle N_{\text{CIV}}/N_{\text{SiIV}} \rangle = 3.98^{+1.15}_{-0.90}$ (the gray shaded region is corresponding $\pm 1\sigma$) from SW09. The red-dash line is $\langle N_{\text{CIV}}/N_{\text{SiIV}} \rangle = 2.5 \pm 0.5$ (the red shaded region is corresponding $\pm 1\sigma$) at $1.5 < |z_P| < 3.3$ kpc from this work.

2011), 3.6 ± 1.3 (Sembach & Savage 1992) and $3.98^{+1.15}_{-0.90}$ (SW09) in the disk-halo interface. The large scatter observed in our data at $|z_P| < 1.5$ kpc and in the literature is typical of this ratio. In a study of 40 sight lines in the disk and disk-halo region, Sembach et al. (1997) found a similar ratio with a large dispersion, $\langle N_{\text{CIV}}/N_{\text{SiIV}} \rangle = 3.8 \pm 1.9$, and noted that in particular

regions, the ratio is significantly higher than the mean, which they attributed to supernova remnants related to Radio Loops I–IV. Similarly, many sight lines through the Carina star-forming region show $N_{\text{CIV}}/N_{\text{SiIV}}$ values significantly and consistently smaller than the Galactic average of $\langle N_{\text{CIV}}/N_{\text{SiIV}} \rangle = 3.9$ (see Figure 17 in Tripp 2022). Additionally, component analyses of absorption lines by Fox et al. (2003), Tripp et al. (2003), Lehner et al. (2011), and Tripp & Song (2012) further support this, revealing large scatters ($\sigma = 1.5$ – 2.7) in $N_{\text{CIV}}/N_{\text{SiIV}}$ values within individual components. These observations suggest that the $N_{\text{CIV}}/N_{\text{SiIV}}$ ratio takes a wide range of values depending on the environment and the physical processes in which C IV and Si IV are created.

While this large scatter in $N_{\text{CIV}}/N_{\text{SiIV}}$ is typical and attributed to the diverse ionization processes creating C IV and Si IV (see Figure 12 in Lehner et al. 2011), our data show a distinct pattern. The majority of our $N_{\text{CIV}}/N_{\text{SiIV}}$ measurements (21 out of 27) cluster around the average $N_{\text{CIV}}/N_{\text{SiIV}} = 2.5$ in the extended disk-halo interface (see the red shaded region in Figure 9), with a significant scatter ($\sigma \geq 1.5$) primarily in the thin disk. This implies that our disk-halo interface sightlines mostly sample gas below the Galactic plane with relatively uniform physical conditions spanning over $0.9 < |z_P| < 3.25$ kpc.

6. DISCUSSION

The main goal of this project is to assess the kinematics, spatial structure, and ionization conditions of the disk-halo interface gas located below the Perseus arm. We detect S II, Si IV, and C IV in the UV spectra of 6 OB stars and 23 AGNs. These sightlines pass below the Perseus arm at mid-arm heights between 70 pc and 3.3 kpc. We discuss the implications of our findings below.

6.1. CGM Contamination to Perseus Absorption is Minimal

An AGN sightline has a significant path length through the Milky Way CGM. Consequently, any absorption from the CGM gas along an AGN sightline may overlap with the foreground Perseus arm absorption. Such CGM contamination could lead to inaccurate measurements of Perseus gas column densities. However, we argue that the measured Perseus gas column densities are free from any CGM contamination based on the following evidence.

Firstly, the estimated Perseus arm column densities toward the AGNs are similar to or smaller than that toward the halo star, PG0122+214 ($|z_P| = 1.9$ kpc). Particularly, in the high ions where $N(z_P)-|z_P|$ distributions are very flat over the whole $|z_P|$ -range, the Perseus

column densities toward most of the AGNs (15 out of 23) are $\geq 1\sigma$ below the halo star sightline (see Figure 7). The 5 AGN sightlines closest in height ($|z_P|=1.8\text{--}2.3$ kpc) to the halo star PG0122+214 show high ion column densities 0.03–0.5 dex and S II column densities ~ 0.2 dex lower than the halo star sightline. Particularly, along the AGN sightline PG0052+251 (at $|z_P|=1.9$ kpc), Si IV and C IV column densities are 0.4 and 0.6 dex smaller than and S II column density is similar to that observed along the halo star sightline PG0122+214. In the presence of substantial low-velocity Milky Way-CGM gas toward these AGN sightlines, one would expect larger column densities toward the AGNs (given the much larger path through the CGM) compared to the halo star sightline, which is not the case. The observed differences in column densities toward the AGNs and the halo star are typical of the inherent column density variability in the Milky Way ISM and disk-halo interface at angular separations of $2\text{--}25^\circ$ (Howk et al. 2002; Tuli et al. 2025 a,b, in preparation).

Secondly, we find $\langle \log N_{\text{Si IV}}/N_{\text{S II}} \rangle = -1.8 \pm 0.2$ in the extraplanar gas at $|z_P| > 1.5$ kpc. Studies of the CGM around Milky-Way mass galaxies show much higher ratios. The CGM of COS-Halos galaxies with similar or higher masses than the Milky Way typically exhibit that the higher ionization states of a species are more prevalent than the lower ones (Werk et al. 2013). Lehner et al. (2020) surveyed the M31 CGM beyond 20 kpc using multiple AGN sightlines and found that S II is not detected with $\langle \log N_{\text{Si IV}}/N_{\text{S II}} \rangle > -1.09$ in all cases, which is $> 4\times$ larger than our measurements. However, Si II, which probe the same gas phase as S II, is mostly detected in M31’s CGM and $N_{\text{Si IV}}/N_{\text{Si II}}$ is better constrained with an average $N_{\text{Si IV}}/N_{\text{Si II}} = -0.15$. In contrast, in the extraplanar Perseus gas at $|z_P| > 1.5$ kpc, we find $[\text{Si IV}/\text{S II}] = \log(N_{\text{Si IV}}/N_{\text{S II}}) - \log(\text{Si}/\text{S})_\odot \equiv -2.2$, further indicating that our survey region is significantly less ionized than expected for the CGM gas.

The consistent column densities of the stellar and AGN sightlines (within the ISM scatter) and the dominance of the low ionization phase in the extraplanar gas at $|z_P| > 1.5$ kpc, therefore, provide compelling evidence that the observed S II, Si IV, and C IV absorption originates from the disk-halo interface gas localized below Perseus arm with negligible contribution from the Milky Way-CGM toward the AGNs.

6.2. CGM Contamination to the Absorption at $|v_{\text{LSR}}| < 100 \text{ km s}^{-1}$ is Minimal

The Milky Way-CGM gas has been traditionally indirectly detected as high velocity clouds (HVCs) at $|v_{\text{LSR}}| > 100 \text{ km s}^{-1}$ in the AGN spectra (Herenz et al.

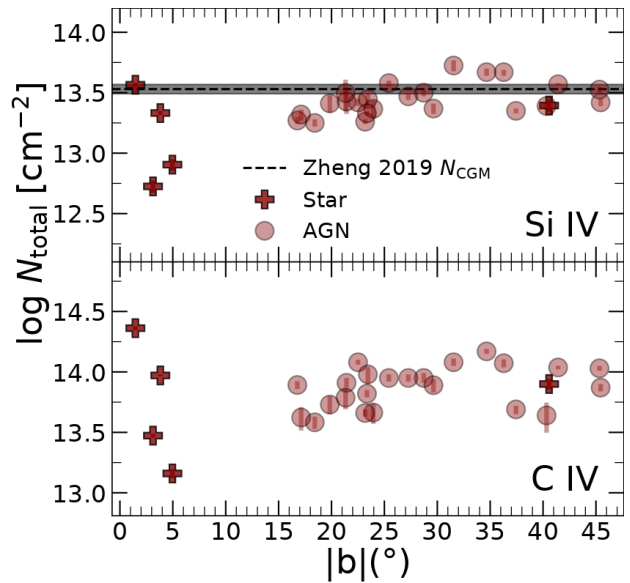


Figure 10. Total integrated Si IV (top) and C IV (bottom) column density (within $|v_{\text{LSR}}| < 100 \text{ km s}^{-1}$) as a function of increasing $|b|$. The gray dash line and the gray shaded box around it are the Zheng et al. (2019) N_{CGM} and its 68% confidence interval.

2013; Richter et al. 2017). However, there is also growing speculation (Zheng et al. 2015, 2020) that a substantial portion (55%–65%) of the warm-hot Milky Way-CGM gas is concealed within the low velocity gas (i.e., the gas with $|v_{\text{LSR}}| < 100 \text{ km s}^{-1}$), traditionally attributed to the nearby Milky Way ISM and disk-halo interface gas. Zheng et al. (2019) modeled the all-sky Si IV column densities toward the AGNs with a 1D (z -dependent) disk-halo interface density distribution (N_{DH}) coupled with a global CGM component (N_{CGM}), such that the average $\log N_{\text{DH}} = 12.11$, and $\log N_{\text{CGM}} = 13.53$. This suggests that the low velocity Si IV absorption toward the AGNs predominantly originates from the Milky Way-CGM gas rather than the disk-halo interface. Subsequent studies using more complex models have argued that the contributions to the Si IV and C IV column densities from the disk-halo interface and the CGM gas are similar, $N_{\text{DH}} \approx N_{\text{CGM}}$ (Qu & Bregman 2019; Qu et al. 2020, 2022). These works collectively suggest that the high ion ISM and disk-halo interface absorption observed along the AGN sightlines include significant contributions from the Milky Way’s CGM.

However, the QuaStar survey (Bish et al. 2021), measured the column densities in the direction of 30 halo star-AGN pairs with angular separations $< 2^\circ$, found minimal excess C IV absorption toward the AGNs compared to the foreground halo stars. They argued that the Milky Way CGM lacks warm gas in general, which

is in contradiction with Zheng et al. (2019), Qu & Bregman (2019) and Qu et al. (2020, 2022). However, Qu et al. (2022) argued that a radially-extended disk, instead of a vertically-extended one, might result in low C IV CGM column densities toward the AGNs.

We find no observable CGM absorption toward the AGNs at the Perseus velocities within $-90 < v_{\text{LSR}} < -25$ (see Section 6.1). In principle the low-velocity absorption in these directions may still include CGM contributions. Therefore, we estimate the Si II, Si IV, and C IV integrated total column densities, N_{total} , within $|v_{\text{LSR}}| < 100 \text{ km s}^{-1}$. Therefore, N_{total} is the column density of the gas between $[-100, 100] \text{ km s}^{-1}$ including Perseus gas. Due to Si II saturation, we focus only on the high ion $N_{\text{total}}-|b|$ distribution (shown in Figure 10). From this Figure, we find: 1) at $|b| > 10^\circ$, none of the high ions shows any trend with increasing $|b|$, and there is a large scatter (~ 0.15 dex) in the data; 2) Si IV N_{total} toward some of the AGNs are within 1σ of Zheng et al. (2019) N_{CGM} , therefore a potential CGM contamination can be present in the $|v_{\text{LSR}}| < 100 \text{ km s}^{-1}$ gas; 3) however, N_{total} toward the AGNs at $|b| \leq 30^\circ$ is consistent with that of the halo star sightline PG0122+214 within 0.1 dex; 3) intriguingly, N_{total} toward the AGNs at $|b| > 30^\circ$ (5 out of 8 measurements) tend to be more than 0.2 dex higher than the halo star sightline (at $|b| \approx 41^\circ$), which is different from the trend seen in the Perseus gas (see Figure 7). It is evident that the higher N_{total} toward the 5 AGNs at $|b| > 30^\circ$ compared to the halo star sightline arise particularly in the gas between -20 and $+50 \text{ km s}^{-1}$. We also notice there is little absorption at $v_{\text{LSR}} > 50 \text{ km s}^{-1}$ toward our AGNs.

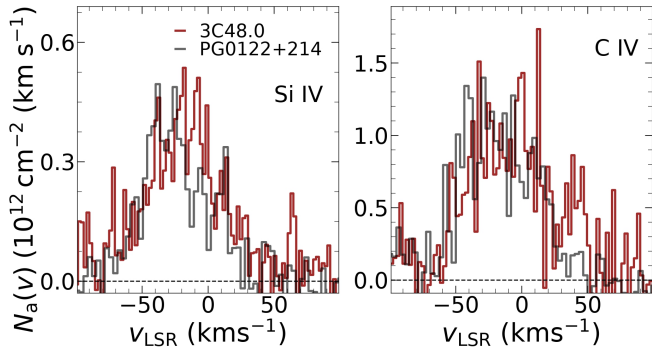


Figure 11. Comparison of the Si IV and C IV $N_a(v)$ profiles toward the AGN 3C48.0 and halo star PG0122+214. These two sightlines pass below the local and Perseus arm material at similar longitudes (133.96° and 133.37° , respectively) but at different latitudes (-28.72° and -40.57° , respectively).

While the excess N_{total} toward the 5 AGNs at $|b| > 30^\circ$ could possibly be attributed to the CGM, another

possibility might be the interception of denser gaseous structures in the local arm by these AGN sightlines. These 5 AGN sightlines are all within $106^\circ < l < 117^\circ$ spanning roughly 15° ($< 130 \text{ pc}$ at $< 0.5 \text{ kpc}$) on the sky. Thus toward these cluster of sightlines, in a narrow segment of the local arm, there could be a local enhancement of gas density. The 3 other AGN sightlines at $|b| > 30^\circ$ are closer in longitude to the halo star and yield similar N_{total} (within the ISM scatter) as the halo star sightline. Particularly, the AGN sightline 3C48.0 $[(l, b) = (133.96^\circ, -28.72^\circ)]$ and the halo star, PG0122+214 $[(l, b) = (133.37^\circ, -40.57^\circ)]$ have very similar longitudes but different latitudes; these two sightlines exhibit similar high ion column densities and show no difference in their high ion $N_a(v)$ profiles, particularly at low velocities (see Figure 11). Moreover, the AGN sightline RXJ0053.7+2232 $[(l, b) = (123.64^\circ, -40.33^\circ)]$, at different longitude but similar latitude as the halo star PG0122+214, also exhibit similar total high ion column density (within the ISM scatter) as the halo star sightline. Each high ion's $N_a(v)$ profiles toward these two sightlines are also similar (see Figure 12).

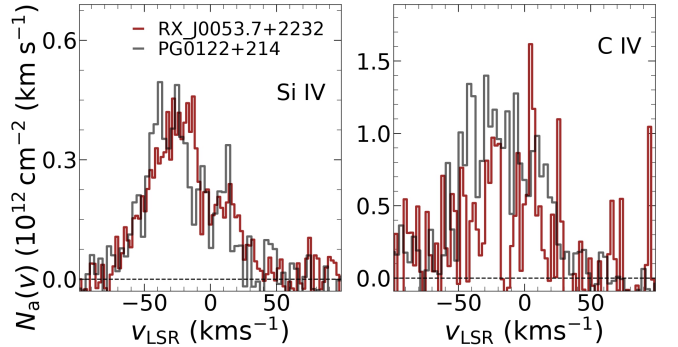


Figure 12. Comparison of the Si IV and C IV $N_a(v)$ profiles toward the AGN RXJ0053.7+2232 and halo star PG0122+214. These two sightlines pass below the local and Perseus arm material at different longitudes (123.64° and 133.37° , respectively) but at similar latitudes (-40.33° and -40.57° , respectively).

Additionally, AGN sightline 3C66A $[(l, b) = (140.14^\circ, -16.77^\circ)]$ and the nearby star HD 14633 $[(l, b) = (140.78^\circ, -18.2^\circ)$ and $D_{\text{star}} = 1.5 \text{ kpc}$] are separated by 1.55° and have total high ion column density consistent within ~ 0.13 dex (typical of ISM scatter at ~ 2 deg angular separation, Tuli et al. 2025 a,b, in preparation). However, these two sightlines' high ion $N_a(v)$ profiles show significant differences over -75 to $+50 \text{ km s}^{-1}$ (see Figure 13). The star is in the inter-arm region, close to the near side of the Perseus arm, whereas the AGN sightline passes over the whole Perseus

arm. We argue that the differences in these sightlines' $N_a(v)$ profiles are due to different path lengths through the Perseus material and not because of the large CGM path length of the AGN sightline, which would result in much larger column density differences than observed between these two sightlines.

These three examples indicate that the column density differences between the AGNs and halo star sightlines originate from the variation in the ISM and disk-halo interface gas distribution rather than from the contamination of the AGN sightlines by the extended CGM gas. We conclude that the high N_{total} toward the cluster of 5 AGNs at $|b| > 30^\circ$ is due to the higher density of the local arm material in these directions. Therefore, the observed trend in the $N_{\text{total}}-|b|$ distributions at $|b| > 30^\circ$ is a bias due to the clustering of those sightlines in a high column density region.

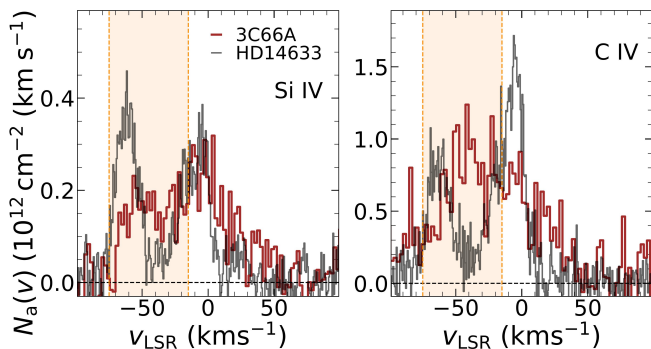


Figure 13. A comparison of the Si IV (left) and C IV (right) $N_a(v)$ profiles toward the AGN 3C66A and the nearby star HD 14633, separated by 1.55° . These two sightlines are at similar longitudes but different latitudes. Unlike the AGN, the star is in the inter-arm region close to the near side of the Perseus arm, and thus lacking the intermediate velocity absorption from most of the Perseus arm, resulting in the observed differences in the $N_a(v)$ profiles over -75 to -15 km s^{-1} (orange shaded region).

We further compare the C IV $\log N|\sin b|$ vs $|b|$ distribution toward the southern halo stars from Bish et al. (2021) (only those with no absorption at $|v_{\text{LSR}}| > 100$ km s^{-1}) to our halo star PG0122+214 and the southern AGN sample from Qu et al. (2022) in Figure 14. The column densities from the halo star sample do not behave differently than the AGN sample. In particular, the column densities toward the southern ($-46^\circ < b < 0^\circ$) AGNs within $95^\circ < l < 145^\circ$ (filled circles in Figure 14) are consistent with those toward the halo stars within the scatter, implying that any CGM absorption along the AGN sightlines is generally quite small. The observed difference in column densities between an AGN

and a halo star sightline in our sample primarily results from the scatter in the foreground ISM and disk-halo interface gas.

In the absence of the Milky Way CGM's contribution in the gas with $|v_{\text{LSR}}| < 100$ km s^{-1} , we can now discuss our results solely in the context of the disk-halo interface gas in the vertical extension of the Perseus arm.

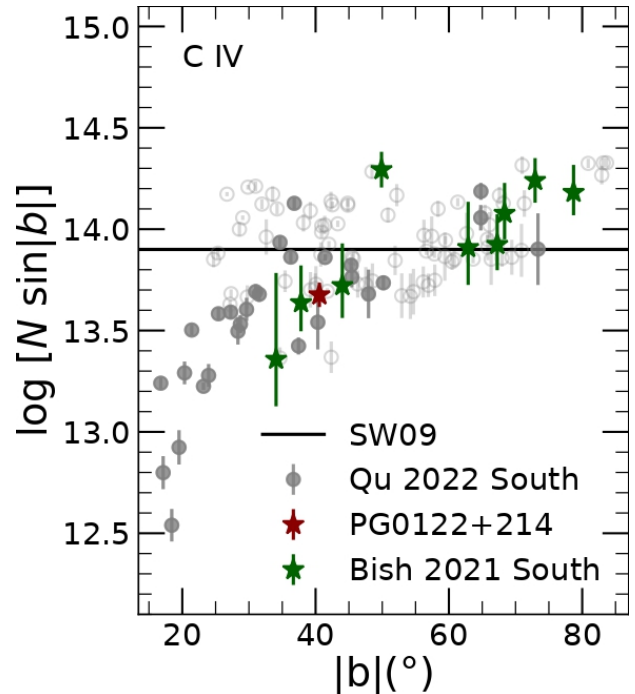


Figure 14. $\log N \sin |b|$ vs $|b|$ distribution of C IV toward the southern AGNs in Qu et al. (2022) (filled and open gray circles), halo stars in Bish et al. (2021) (green stars) and our halo star (red star). The filled gray circles are the Qu et al. (2022) southern AGN measurements within $95^\circ < l < 145^\circ$, the longitude range used in our work. Column density measurements toward the halo stars are consistent with the measurements toward the AGN.

6.3. A Complex Spatial Structure with Distinct Physical Conditions below the Perseus Arm

As mentioned previously, using the diffuse emission from the warm neutral and ionized medium, as well as absorption spectra of hundreds of halo star sightlines (and a handful of AGN sightlines) throughout the Galaxy, early surveys predicted simple exponential gas distribution in the disk-halo interface, i.e., the flat slab model, with temperature-dependent scale heights of the different gas phases (Lockman et al. 1986; Dickey & Lockman 1990; Haffner et al. 1999; Bowen et al. 2008; Savage & Wakker 2009). However, more recent works using hundreds of AGN sightlines reported that the disk-

halo interface absorption toward the AGNs, particularly in the transition temperature ions, might suffer contamination from the low velocity ($|v_{\text{LSR}}| < 100 \text{ km s}^{-1}$) CGM gas, therefore requiring more complex models that include a global CGM component as well as the exponential disk-halo interface model to explain the observed column densities toward the AGNs (Zheng et al. 2019; Qu & Bregman 2019; Qu et al. 2020, 2022). Our experiment avoids the ambiguities created by using total integrated sightline column densities, $N(< z)$, by assessing the column density distribution, $N(z_{\text{P}})$, directly below the Perseus arm at heights between $|z_{\text{P}}| = 70 \text{ pc}$ and 3.3 kpc using 6 stellar and 23 AGN sightlines. Our experiment sheds light on the vertical structure, kinematics, and ionization condition of the disk-halo interface gas below the Perseus arm.

We detect a significant amount of H I, S II, Si IV, and C IV up to 3.3 kpc below the Perseus arm. We find that the vertical structure of the Perseus arm is complex, particularly for the neutral/low ionization gas. H I and S II column densities decline sharply up to $|z_{\text{P}}| = 1.5 \text{ kpc}$, and over $|z_{\text{P}}| = 1.5\text{--}3.3 \text{ kpc}$, their $N(z_{\text{P}})\text{--}|z_{\text{P}}|$ distributions are very flat—significantly deviating from the flat slab fits of the earlier works (see Figure 7). Additionally, H I and S II $N(z_{\text{P}})\text{--}|z_{\text{P}}|$ distributions are significantly different from the high ionization gas, also reported by SW09. Like SW09, we find the high ion $N(z_{\text{P}})\text{--}|z_{\text{P}}|$ distributions are very flat for the entire range of $|z_{\text{P}}|$ probed by our sample (see 7). A single exponential scale height model provides a poor fit for H I and S II, whereas the highly ionized gas distribution may be exponential, but a scale height $h_z > 3 \text{ kpc}$ is required (see Table 4).

To gain more insight into disk-halo interface gas below the Perseus arm, we investigate the gas kinematics. We find that the high and low ionization gas kinematics resemble the Galactic rotation, roughly spanning over -20 to -75 km s^{-1} . Any vertical fountain flow of roughly few tens of km s^{-1} (Kim et al. 2017) have a small ($10\text{--}20 \text{ km s}^{-1}$) projected line of sight velocity along the disk-halo interface sightlines, which is possibly offset by the projected halo rotation lagging behind the disk rotation. The lack of vertical motion in the gas may also imply that any past fountain flow has significantly slowed down over time, and feedback in this arm region may be currently quiescent. Therefore, our data, particularly in the disk-halo interface sightlines, are unable to capture any vertical motion or rotation lag in the gas below the Perseus arm.

Another key finding is the changing physical and ionization conditions of the Perseus arm gas from the thin disk to the disk-halo interface. We find: 1) in the thin disk, the low and high ionization gas kinematics are very

different; however, they are very similar in the disk-halo interface; 2) $N_{\text{Si IV}}/N_{\text{S II}}$ values increase from the thin disk to the disk-halo interface and do not vary at all with height in the disk-halo interface; 3) $N_{\text{C IV}}/N_{\text{Si IV}}$ values also do not vary at all with height in the disk-halo interface, and the observed scatter in this ratio significantly decreases from the thin disk to the disk-halo interface. These observations indicate that the processes governing the low and high ionization gas phases are very different in the thin disk than in the disk-halo interface.

Secondly, we measure $\langle \log N_{\text{Si IV}}/N_{\text{S II}} \rangle = -1.8$ in the disk-halo interface gas below the Perseus arm, implying the S II column density on average is ~ 60 times higher than Si IV—this is very different from the typical ionization state of the CGM gas observed at low impact parameter ($< 15 \text{ kpc}$) in the M31 and other galaxies (Lehner et al. 2020; Werk et al. 2013). S II is primarily produced in the warm neutral medium (WNM) (with ionization fraction, $\chi_{\text{S II}} = 1$) and the warm ionized medium (WIM) ($\chi_{\text{S II}} = 0.8$) (Howk et al. 2006; Howk & Consiglio 2012). In contrast, Si IV predominantly resides in the more ionized and hotter, $10^{4.2}\text{--}10^{5.1} \text{ K}$, gas phase with $\chi_{\text{Si IV}} \leq 0.38$ under collisional ionization equilibrium (CIE) conditions ($\chi_{\text{Si IV}} \leq 0.06$ for non-equilibrium collisional ionization, NECI) (Gnat & Sternberg 2007). Using the average column density, $N(\text{X})$, in the extended disk-halo interface ($|z_{\text{P}}| > 1.5 \text{ kpc}$), ion fraction, $\chi(\text{X})$, and assuming solar abundance, $A(\text{X})$ (Asplund et al. 2009), we can estimate the associated hydrogen column density of a gas phase traced by the ion, X, e.g. $N(\text{H})_{\text{X}} = N(\text{X})A(\text{X})^{-1}\chi(\text{X})^{-1}$. We find: 1) $\log N(\text{H})_{\text{S II}} = 19.7$, which represents $N(\text{H})$ in the WNM+WIM gas; 2) $N(\text{H})_{\text{Si IV}} > 17.8$ for CIE, > 18.6 for NECI. The average $\log N(\text{HI}) = 19.5$ at $|z_{\text{P}}| > 1.5 \text{ kpc}$ in this work represents the WNM. Therefore, in the extended disk-halo interface below the Perseus arm, the WIM gas $\log N(\text{H})$ is 19.3, implying that the WNM is dominant over the WIM. However, $\log N(\text{H})_{\text{Si IV}}$ is unconstrained in this work and a hot (O VII-bearing) phase could be comparably or even more dominant which is also unconstrained in this dataset.

Thirdly, we find that $\langle N_{\text{C IV}}/N_{\text{Si IV}} \rangle = 2.5 \pm 0.5$ in the disk-halo interface gas at $|z_{\text{P}}| > 1.5 \text{ kpc}$. The two aspects of this observed ratio are: a) it is below the Galactic average of 3.98; and b) it has a significantly smaller scatter (0.5) than typically observed (~ 2 , e.g., Fox et al. 2003; Tripp et al. 2003; Lehner et al. 2011; Tripp & Song 2012)—indicating that our sightlines are probing similar physical conditions in the extraplanar gas spanning over $0.9 < |z_{\text{P}}| < 3.25 \text{ kpc}$ (see Figure 9). Theoretically, several models depending on the gas temperature can produce the observed low $N_{\text{C IV}}/N_{\text{Si IV}}$ in

the disk-halo interface below the Perseus arm (see Figure 12 [Lehner et al. 2011](#)). An NCIE ([Gnat & Sternberg 2007](#)) or shock ionization (SI) model ([Gnat & Sternberg 2009](#)) can reproduce the observed low $N_{\text{C IV}}/N_{\text{Si IV}}$ values at gas temperature $T = 2 \times 10^4$ K. Alternatively, a CIE model ([Gnat & Sternberg 2007](#)) with gas temperature $T = 7 \times 10^4$ K or a turbulent mixing layer (TML) model with 25 km s^{-1} velocity shear ([Slavin et al. 1993](#)) at gas temperature $T = 1.6 \times 10^5$ K can also produce the observed low $N_{\text{C IV}}/N_{\text{Si IV}}$ values. Similarly, cooling flows from the hot ($> 10^6$ K) phase to the cool phase (10^4 K) can produce the C IV/Si IV values observed in the disk-halo interface below the Perseus arm in this work, however we also need to measure the other high ion ratios e.g., C IV/O VI, and O VI/N V to constrain these models ([Wakker et al. 2012](#); [Tripp 2022](#)). Additionally, the observed kinematic similarities between the low and high ionization gas suggest that C IV and Si IV is residing in the mixing layers or interfaces between the hot ($> 10^6$ K) and S II bearing cool (10^4 K) gas phases; however the existing interface or mixing layer models typically predict higher C IV/Si IV ratio than we have observed (see Figure 18 [Tripp 2022](#)). While all of these aforementioned processes can be traced back to the interaction of the energetic hot feedback material with its surroundings, it is evident from [Lehner et al. \(2011\)](#) Figure 12 that the observed disk-halo interface $N_{\text{C IV}}/N_{\text{Si IV}}$ values are incompatible with the models of photoionizing radiation from the hot stars or the cooling hot plasma. To better understand the physical origin of the highly ionized gas in the southern vertical extension of the Perseus arm we would need to constrain the gas temperature by component fitting of the ISM absorption lines and properly accounting for any turbulent motion in the gas.

With minimal contribution from the low-velocity Milky Way-CGM gas along our AGN sightlines, the observed spatial structure and ionization conditions in the disk-halo interface below the Perseus arm may be a consequence of stellar feedback from the arm or material accretion into the arm from the CGM. Our survey excludes regions below the arm where infalling IVCs were detected in H I 21 cm emission (see Figure 12 of [Wakker 2001](#)); however, a detailed metallicity assessment in this region could further provide useful constraints. Our sightlines pass through regions of multiple supernova remnants, super-bubbles, and supershells located in and below the arm ([Thornton et al. 1998](#); [Suad et al. 2014](#)). These structures can influence the gas distribution below the Perseus arm by propelling a substantial amount of arm material to considerable heights. The lack of vertical motion in the gas may indicate that the ejected foun-

tain gas has significantly slowed down over time. Such phenomena are characteristic of all spiral arms, where Galactic fountains/chimneys occur frequently ([Bregman 1980](#); [Norman & Ikeuchi 1989](#); [Kim et al. 2017](#); [Kim & Ostriker 2018](#))—consequently significantly altering the disk-halo interface’s gas distribution and ionization conditions locally above/below the arms.

7. SUMMARY

Using HST STIS and COS UV absorption spectroscopy of 6 stars and 23 AGNs projected behind the Perseus arm within $95^\circ < l < 145^\circ$, and $|b| < 46^\circ$, we detect S II, Si IV, C IV and the associated H I 21 cm emission in the disk-halo interface below the Perseus arm. Our key findings are:

1. We have detected warm-hot disk-halo interface material between 70 pc and 3.3 kpc below the Perseus arm. Our AGN sightlines show negligible contribution from the $|v_{\text{LSR}}| < 100 \text{ km s}^{-1}$ CGM gas, implying that all of the absorption along the AGN sightlines is arising from the thin disk and disk-halo interface. C IV and Si IV (total integrated and Perseus) column densities along the AGN sightlines are consistent with that of the halo star sightline within the typical Milky Way ISM column density variation (~ 0.2 – 0.3 dex).
2. The neutral and low ionization gas’s density distribution below the Perseus arm is complex. H I and S II column densities sharply drop with $|z_{\text{P}}|$ up to 1.5 kpc and do not vary much after. In contrast, high ion column density does not vary at all over the whole $|z_{\text{P}}|$ range probed by our sample. Our data show that H I and S II column densities do not conform to single exponential distributions; however, C IV and Si IV column densities may follow simple exponential distributions with possibly larger scale heights than [SW09](#). Highly ionized gas’s density distribution significantly differs from the neutral and low ionization gas below the Perseus arm.
3. Below the Perseus arm, disk-halo interface gas kinematics purely follow Galactic rotation. This suggests limited fountain speed in the disk-halo interface gas, making its kinematic imprint minimal in our data—implying that feedback is currently quiescent in this region, and any past fountain flow has sufficiently slowed down.
4. We find the disk-halo interface gas below Perseus arm is predominantly WNM gas with associated

$\log N(\text{H}) = 19.5$. WIM $\log N(\text{H})$ is 19.3. Additionally, S II column density in the disk-halo interface, 0.5–3.3 kpc below Perseus arm, is on average 60 times higher than Si IV. However, the $\log N(\text{H})$ in the highly ionized gas is unconstrained in this work.

5. We notice a changing ionization condition from the thin disk to the disk-halo interface gas below the Perseus arm as indicated by the 1) increasing $N_{\text{SiIV}}/N_{\text{SII}}$ values from the thin disk to the disk-halo interface; 2) kinematic alignment of S II $N_a(v)$ profiles with the high ion profiles in the disk-halo interface which is not the case in the thin disk; and 3) the decreasing scatter in the $N_{\text{CIV}}/N_{\text{SiIV}}$ values from the thin disk to the disk-halo interface.
6. In the disk-halo interface, we observe similar conditions as indicated by non-varying $N_{\text{SiIV}}/N_{\text{SII}}$ and $N_{\text{CIV}}/N_{\text{SiIV}}$ values in the disk-halo interface sightlines. Additionally, S II is co-spatial with

the high ions in the disk-halo interface below the Perseus arm implying that the high ions may reside in the turbulent mixing layers at the interfaces between the coronal gas at $T > 10^6$ K and the S II bearing $T = 10^4$ K gas.

- 1 Support for this research was provided by NASA
- 2 through grant HST-GO-14602 from the Space Telescope
- 3 Science Institute, which is operated by the Association
- 4 of Universities for Research in Astronomy, Incorporated,
- 5 under NASA contract NAS5-26555. This research has
- 6 made extensive use of the NASA Astrophysics Data Sys-
- 7 tem Abstract Service and the Centre de Donn´ees de
- 8 Strasbourg (CDS).

- 9 *Software:* Adstex, Astropy (Astropy Collaboration
- 10 et al. 2013, 2018, 2022), Emcee (Foreman-Mackey et al.
- 11 2013), Matplotlib (Hunter 2007), Scipy (Virtanen et al.
- 12 2020) .

REFERENCES

- Albert, C. E., & Danly, L. 2004, in *Astrophysics and Space Science Library*, Vol. 312, High Velocity Clouds, ed. H. van Woerden, B. P. Wakker, U. J. Schwarz, & K. S. de Boer, 73
- Asplund, M., Grevesse, N., Sauval, A. J., & Scott, P. 2009, *ARA&A*, 47, 481, doi: [10.1146/annurev.astro.46.060407.145222](https://doi.org/10.1146/annurev.astro.46.060407.145222)
- Astropy Collaboration, Robitaille, T. P., Tollerud, E. J., et al. 2013, *A&A*, 558, A33, doi: [10.1051/0004-6361/201322068](https://doi.org/10.1051/0004-6361/201322068)
- Astropy Collaboration, Price-Whelan, A. M., Sipőcz, B. M., et al. 2018, *AJ*, 156, 123, doi: [10.3847/1538-3881/aabc4f](https://doi.org/10.3847/1538-3881/aabc4f)
- Astropy Collaboration, Price-Whelan, A. M., Lim, P. L., et al. 2022, *ApJ*, 935, 167, doi: [10.3847/1538-4357/ac7c74](https://doi.org/10.3847/1538-4357/ac7c74)
- Bish, H. V., Werk, J. K., Peek, J., Zheng, Y., & Putman, M. 2021, *ApJ*, 912, 8, doi: [10.3847/1538-4357/abeb6b](https://doi.org/10.3847/1538-4357/abeb6b)
- Bizyaev, D., Waltherbos, R. A. M., Yoachim, P., et al. 2017, *ApJ*, 839, 87, doi: [10.3847/1538-4357/aa6979](https://doi.org/10.3847/1538-4357/aa6979)
- Bowen, D. V., Jenkins, E. B., Tripp, T. M., et al. 2008, *ApJS*, 176, 59, doi: [10.1086/524773](https://doi.org/10.1086/524773)
- Brandt, J. C., Heap, S. R., Beaver, E. A., et al. 1999, *AJ*, 117, 400, doi: [10.1086/300673](https://doi.org/10.1086/300673)
- Branton, D., & Riley, A. 2021, in *STIS Instrument Handbook for Cycle 29 v. 20*, Vol. 20, 20
- Bregman, J. N. 1980, *ApJ*, 236, 577, doi: [10.1086/157776](https://doi.org/10.1086/157776)
- Burton, W. B. 1971, *A&A*, 10, 76
- Choi, Y. K., Hachisuka, K., Reid, M. J., et al. 2014, *ApJ*, 790, 99, doi: [10.1088/0004-637X/790/2/99](https://doi.org/10.1088/0004-637X/790/2/99)
- Dame, T. M., Ungerechts, H., Cohen, R. S., et al. 1987, *ApJ*, 322, 706, doi: [10.1086/165766](https://doi.org/10.1086/165766)
- Dickey, J. M., & Lockman, F. J. 1990, *ARA&A*, 28, 215, doi: [10.1146/annurev.aa.28.090190.001243](https://doi.org/10.1146/annurev.aa.28.090190.001243)
- Diplas, A., & Savage, B. D. 1994, *ApJS*, 93, 211, doi: [10.1086/192052](https://doi.org/10.1086/192052)
- Du, X., Xu, Y., Yang, J., et al. 2016, *ApJS*, 224, 7, doi: [10.3847/0067-0049/224/1/7](https://doi.org/10.3847/0067-0049/224/1/7)
- Elmegreen, B. G. 2011, in *EAS Publications Series*, Vol. 51, *EAS Publications Series*, ed. C. Charbonnel & T. Montmerle, 19–30, doi: [10.1051/eas/1151002](https://doi.org/10.1051/eas/1151002)
- Fitzpatrick, E. L., & Spitzer, Lyman, J. 1994, *ApJ*, 427, 232, doi: [10.1086/174136](https://doi.org/10.1086/174136)
- . 1997, *ApJ*, 475, 623, doi: [10.1086/303556](https://doi.org/10.1086/303556)
- Foreman-Mackey, D., Hogg, D. W., Lang, D., & Goodman, J. 2013, *PASP*, 125, 306, doi: [10.1086/670067](https://doi.org/10.1086/670067)
- Fox, A. J., Savage, B. D., Sembach, K. R., et al. 2003, *ApJ*, 582, 793, doi: [10.1086/344692](https://doi.org/10.1086/344692)
- Gentile, G., Józsa, G. I. G., Serra, P., et al. 2013, *A&A*, 554, A125, doi: [10.1051/0004-6361/201321116](https://doi.org/10.1051/0004-6361/201321116)
- Gnat, O., & Sternberg, A. 2007, in *American Astronomical Society Meeting Abstracts*, Vol. 210, *American Astronomical Society Meeting Abstracts #210*, 113.08
- Gnat, O., & Sternberg, A. 2009, *ApJ*, 693, 1514, doi: [10.1088/0004-637X/693/2/1514](https://doi.org/10.1088/0004-637X/693/2/1514)
- Haffner, L. M., Reynolds, R. J., & Tufte, S. L. 1999, *ApJ*, 523, 223, doi: [10.1086/307734](https://doi.org/10.1086/307734)

- Heckman, T. M. 2002, in *Astronomical Society of the Pacific Conference Series*, Vol. 254, *Extragalactic Gas at Low Redshift*, ed. J. S. Mulchaey & J. T. Stocke, 292, doi: [10.48550/arXiv.astro-ph/0107438](https://doi.org/10.48550/arXiv.astro-ph/0107438)
- Herenz, P., Richter, P., Charlton, J. C., & Masiero, J. R. 2013, *A&A*, 550, A87, doi: [10.1051/0004-6361/201220531](https://doi.org/10.1051/0004-6361/201220531)
- Howk, J. C., & Consiglio, S. M. 2012, *ApJ*, 759, 97, doi: [10.1088/0004-637X/759/2/97](https://doi.org/10.1088/0004-637X/759/2/97)
- Howk, J. C., Savage, B. D., & Fabian, D. 1999, *ApJ*, 525, 253, doi: [10.1086/307888](https://doi.org/10.1086/307888)
- Howk, J. C., Savage, B. D., Sembach, K. R., & Hoopes, C. G. 2002, *ApJ*, 572, 264, doi: [10.1086/340231](https://doi.org/10.1086/340231)
- Howk, J. C., Sembach, K. R., & Savage, B. D. 2006, *ApJ*, 637, 333, doi: [10.1086/497352](https://doi.org/10.1086/497352)
- Humphreys, R. M. 1978, *ApJS*, 38, 309, doi: [10.1086/190559](https://doi.org/10.1086/190559)
- Hunter, J. D. 2007, *Computing in Science and Engineering*, 9, 90, doi: [10.1109/MCSE.2007.55](https://doi.org/10.1109/MCSE.2007.55)
- Kepner, M. 1970, *A&A*, 5, 444
- Kerr, F. J., Hindman, J. V., & Carpenter, M. S. 1957, *Nature*, 180, 677, doi: [10.1038/180677a0](https://doi.org/10.1038/180677a0)
- Kim, C.-G., & Ostriker, E. C. 2018, *ApJ*, 853, 173, doi: [10.3847/1538-4357/aaa5ff](https://doi.org/10.3847/1538-4357/aaa5ff)
- Kim, C.-G., Ostriker, E. C., & Raileanu, R. 2017, *ApJ*, 834, 25, doi: [10.3847/1538-4357/834/1/25](https://doi.org/10.3847/1538-4357/834/1/25)
- Kimble, R. A., Woodgate, B. E., Bowers, C. W., et al. 1998, *ApJL*, 492, L83, doi: [10.1086/311102](https://doi.org/10.1086/311102)
- Krishnarao, D., Haffner, L. M., Benjamin, R. A., Hill, A. S., & Barger, K. A. 2017, *ApJ*, 838, 43, doi: [10.3847/1538-4357/aa63e6](https://doi.org/10.3847/1538-4357/aa63e6)
- Kuntz, K. D., & Danly, L. 1996, *ApJ*, 457, 703, doi: [10.1086/176765](https://doi.org/10.1086/176765)
- Lehner, N., Howk, J. C., Marasco, A., & Fraternali, F. 2022, *MNRAS*, 513, 3228, doi: [10.1093/mnras/stac987](https://doi.org/10.1093/mnras/stac987)
- Lehner, N., Zech, W. F., Howk, J. C., & Savage, B. D. 2011, *ApJ*, 727, 46, doi: [10.1088/0004-637X/727/1/46](https://doi.org/10.1088/0004-637X/727/1/46)
- Lehner, N., Berek, S. C., Howk, J. C., et al. 2020, *ApJ*, 900, 9, doi: [10.3847/1538-4357/aba49c](https://doi.org/10.3847/1538-4357/aba49c)
- Levy, R. C., Bolatto, A. D., Sánchez, S. F., et al. 2019, *ApJ*, 882, 84, doi: [10.3847/1538-4357/ab2ed4](https://doi.org/10.3847/1538-4357/ab2ed4)
- Lindegren, L., Klioner, S. A., Hernández, J., et al. 2021, *A&A*, 649, A2, doi: [10.1051/0004-6361/202039709](https://doi.org/10.1051/0004-6361/202039709)
- Lockman, F. J., Hobbs, L. M., & Shull, J. M. 1986, *ApJ*, 301, 380, doi: [10.1086/163907](https://doi.org/10.1086/163907)
- Maíz-Apellániz, J., Walborn, N. R., Galué, H. Á., & Wei, L. H. 2004, *ApJS*, 151, 103, doi: [10.1086/381380](https://doi.org/10.1086/381380)
- Marasco, A., Fraternali, F., Lehner, N., & Howk, J. C. 2022, *MNRAS*, 515, 4176, doi: [10.1093/mnras/stac1172](https://doi.org/10.1093/mnras/stac1172)
- McKee, C. F., & Ostriker, E. C. 2007, *ARA&A*, 45, 565, doi: [10.1146/annurev.astro.45.051806.110602](https://doi.org/10.1146/annurev.astro.45.051806.110602)
- Miville-Deschênes, M.-A., Murray, N., & Lee, E. J. 2017, *ApJ*, 834, 57, doi: [10.3847/1538-4357/834/1/57](https://doi.org/10.3847/1538-4357/834/1/57)
- Morgan, W. W., Code, A. D., & Whitford, A. E. 1955, *ApJS*, 2, 41, doi: [10.1086/190016](https://doi.org/10.1086/190016)
- Norman, C. A., & Ikeuchi, S. 1989, *ApJ*, 345, 372, doi: [10.1086/167912](https://doi.org/10.1086/167912)
- Ojha, D. K. 2001, *MNRAS*, 322, 426, doi: [10.1046/j.1365-8711.2001.04155.x](https://doi.org/10.1046/j.1365-8711.2001.04155.x)
- Oort, J. H., Kerr, F. J., & Westerhout, G. 1958, *MNRAS*, 118, 379, doi: [10.1093/mnras/118.4.379](https://doi.org/10.1093/mnras/118.4.379)
- Peek, J. E. G., Tchernyshyov, K., & Miville-Deschenes, M.-A. 2022, *ApJ*, 925, 201, doi: [10.3847/1538-4357/ac3f34](https://doi.org/10.3847/1538-4357/ac3f34)
- Putman, M. E., Peek, J. E. G., & Heitsch, F. 2009, *arXiv e-prints*, arXiv:0907.1023, doi: [10.48550/arXiv.0907.1023](https://doi.org/10.48550/arXiv.0907.1023)
- Putman, M. E., Peek, J. E. G., & Joung, M. R. 2012, *ARA&A*, 50, 491, doi: [10.1146/annurev-astro-081811-125612](https://doi.org/10.1146/annurev-astro-081811-125612)
- Qu, Z., & Bregman, J. N. 2019, *ApJ*, 880, 89, doi: [10.3847/1538-4357/ab2a0b](https://doi.org/10.3847/1538-4357/ab2a0b)
- Qu, Z., Bregman, J. N., Hodges-Kluck, E., Li, J.-T., & Lindley, R. 2020, *ApJ*, 894, 142, doi: [10.3847/1538-4357/ab774e](https://doi.org/10.3847/1538-4357/ab774e)
- Qu, Z., Lindley, R., & Bregman, J. N. 2022, *ApJ*, 924, 86, doi: [10.3847/1538-4357/ac35cd](https://doi.org/10.3847/1538-4357/ac35cd)
- Ramspeck, M., Heber, U., & Moehler, S. 2001, *A&A*, 378, 907, doi: [10.1051/0004-6361:20011246](https://doi.org/10.1051/0004-6361:20011246)
- Reid, M. J., Dame, T. M., Menten, K. M., & Brunthaler, A. 2016, *ApJ*, 823, 77, doi: [10.3847/0004-637X/823/2/77](https://doi.org/10.3847/0004-637X/823/2/77)
- Reid, M. J., Menten, K. M., Zheng, X. W., et al. 2009, *ApJ*, 700, 137, doi: [10.1088/0004-637X/700/1/13710.48550/arXiv.0902.3913](https://doi.org/10.1088/0004-637X/700/1/13710.48550/arXiv.0902.3913)
- Reid, M. J., Menten, K. M., Brunthaler, A., et al. 2014, *ApJ*, 783, 130, doi: [10.1088/0004-637X/783/2/130](https://doi.org/10.1088/0004-637X/783/2/130)
- . 2019, *ApJ*, 885, 131, doi: [10.3847/1538-4357/ab4a11](https://doi.org/10.3847/1538-4357/ab4a11)
- Richter, P., Sembach, K. R., Wakker, B. P., et al. 2001, *ApJ*, 559, 318, doi: [10.1086/322401](https://doi.org/10.1086/322401)
- Richter, P., Nuza, S. E., Fox, A. J., et al. 2017, *A&A*, 607, A48, doi: [10.1051/0004-6361/201630081](https://doi.org/10.1051/0004-6361/201630081)
- Savage, B. D., & Massa, D. 1985, *ApJL*, 295, L9, doi: [10.1086/184527](https://doi.org/10.1086/184527)
- Savage, B. D., & Sembach, K. R. 1991, *ApJ*, 379, 245, doi: [10.1086/170498](https://doi.org/10.1086/170498)
- Savage, B. D., Sembach, K. R., & Lu, L. 1997, *AJ*, 113, 2158, doi: [10.1086/118427](https://doi.org/10.1086/118427)
- Savage, B. D., & Wakker, B. P. 2009, *ApJ*, 702, 1472, doi: [10.1088/0004-637X/702/2/1472](https://doi.org/10.1088/0004-637X/702/2/1472)
- Savage, B. D., Sembach, K. R., Wakker, B. P., et al. 2003, *ApJS*, 146, 125, doi: [10.1086/346229](https://doi.org/10.1086/346229)

- Sembach, K. R., & Savage, B. D. 1992, *ApJS*, 83, 147, doi: [10.1086/191734](https://doi.org/10.1086/191734)
- . 1994, *ApJ*, 431, 201, doi: [10.1086/174478](https://doi.org/10.1086/174478)
- Sembach, K. R., Savage, B. D., & Lu, L. 1995, *ApJ*, 439, 672, doi: [10.1086/175206](https://doi.org/10.1086/175206)
- Sembach, K. R., Savage, B. D., & Tripp, T. M. 1997, *ApJ*, 480, 216, doi: [10.1086/303956](https://doi.org/10.1086/303956)
- Shapiro, P. R., & Field, G. B. 1976, *ApJ*, 205, 762, doi: [10.1086/154332](https://doi.org/10.1086/154332)
- Slavin, J. D., Shull, J. M., & Begelman, M. C. 1993, *ApJ*, 407, 83, doi: [10.1086/172494](https://doi.org/10.1086/172494)
- Söding, L., Edenhofer, G., Enßlin, T. A., et al. 2024, arXiv e-prints, arXiv:2407.02859, doi: [10.48550/arXiv.2407.02859](https://doi.org/10.48550/arXiv.2407.02859)
- Sofue, Y., & Tosa, M. 1974, *A&A*, 36, 237
- Spitzer, Lyman, J., & Fitzpatrick, E. L. 1992, *ApJL*, 391, L41, doi: [10.1086/186394](https://doi.org/10.1086/186394)
- . 1993, *ApJ*, 409, 299, doi: [10.1086/172664](https://doi.org/10.1086/172664)
- Suad, L. A., Caiafa, C. F., Arnal, E. M., & Cichowolski, S. 2014, *A&A*, 564, A116, doi: [10.1051/0004-6361/201323147](https://doi.org/10.1051/0004-6361/201323147)
- Thompson, T. A., & Heckman, T. M. 2024, *ARA&A*, 62, 529, doi: [10.1146/annurev-astro-041224-011924](https://doi.org/10.1146/annurev-astro-041224-011924)
- Thornton, K., Gaudlitz, M., Janka, H. T., & Steinmetz, M. 1998, *ApJ*, 500, 95, doi: [10.1086/305704](https://doi.org/10.1086/305704)
- Tripp, T. M. 2022, *MNRAS*, 511, 1714, doi: [10.1093/mnras/stac044](https://doi.org/10.1093/mnras/stac044)
- Tripp, T. M., & Song, L. 2012, *ApJ*, 746, 173, doi: [10.1088/0004-637X/746/2/173](https://doi.org/10.1088/0004-637X/746/2/173)
- Tripp, T. M., Wakker, B. P., Jenkins, E. B., et al. 2003, *AJ*, 125, 3122, doi: [10.1086/374995](https://doi.org/10.1086/374995)
- Verschuur, G. L. 1973, *A&A*, 24, 193
- Virtanen, P., Gommers, R., Oliphant, T. E., et al. 2020, *Nature Methods*, 17, 261, doi: [10.1038/s41592-019-0686-2](https://doi.org/10.1038/s41592-019-0686-2)
- Wakker, B. P. 2001, *ApJS*, 136, 463, doi: [10.1086/321783](https://doi.org/10.1086/321783)
- Wakker, B. P., Savage, B. D., Fox, A. J., Benjamin, R. A., & Shapiro, P. R. 2012, *ApJ*, 749, 157, doi: [10.1088/0004-637X/749/2/157](https://doi.org/10.1088/0004-637X/749/2/157)
- Walborn, N. R. 1972, *AJ*, 77, 312, doi: [10.1086/111285](https://doi.org/10.1086/111285)
- . 1973, *AJ*, 78, 1067, doi: [10.1086/111509](https://doi.org/10.1086/111509)
- Werk, J. K., Prochaska, J. X., Thom, C., et al. 2013, *ApJS*, 204, 17, doi: [10.1088/0067-0049/204/2/17](https://doi.org/10.1088/0067-0049/204/2/17)
- Winkel, B., Kalberla, P. M. W., Kerp, J., & Flöer, L. 2010, *ApJS*, 188, 488, doi: [10.1088/0067-0049/188/2/488](https://doi.org/10.1088/0067-0049/188/2/488)
- Woodgate, B. E., Kimble, R. A., Bowers, C. W., et al. 1998, *PASP*, 110, 1183, doi: [10.1086/316243](https://doi.org/10.1086/316243)
- Wotta, C. B., Lehner, N., Howk, J. C., O’Meara, J. M., & Prochaska, J. X. 2016, *ApJ*, 831, 95, doi: [10.3847/0004-637X/831/1/95](https://doi.org/10.3847/0004-637X/831/1/95)
- Xu, Y., Hao, C. J., Liu, D. J., et al. 2023, *ApJ*, 947, 54, doi: [10.3847/1538-4357/acc45c](https://doi.org/10.3847/1538-4357/acc45c)
- Xu, Y., Bian, S. B., Reid, M. J., et al. 2018, *A&A*, 616, L15, doi: [10.1051/0004-6361/201833407](https://doi.org/10.1051/0004-6361/201833407)
- Yao, Y., & Wang, Q. D. 2005, *ApJ*, 624, 751, doi: [10.1086/429537](https://doi.org/10.1086/429537)
- Zheng, Y., Peek, J. E. G., Putman, M. E., & Werk, J. K. 2019, *ApJ*, 871, 35, doi: [10.3847/1538-4357/aaf6eb](https://doi.org/10.3847/1538-4357/aaf6eb)
- Zheng, Y., Putman, M. E., Peek, J. E. G., & Joung, M. R. 2015, *ApJ*, 807, 103, doi: [10.1088/0004-637X/807/1/103](https://doi.org/10.1088/0004-637X/807/1/103)
- Zheng, Y., Peebles, M. S., O’Shea, B. W., et al. 2020, *ApJ*, 896, 143, doi: [10.3847/1538-4357/ab960a](https://doi.org/10.3847/1538-4357/ab960a)
- Zschaechner, L. K., & Rand, R. J. 2015, *ApJ*, 808, 153, doi: [10.1088/0004-637X/808/2/153](https://doi.org/10.1088/0004-637X/808/2/153)

APPENDIX

A. SUMMARY FIGURE

Figure 15 shows the raw flux and continuum model (yellow solid line) (*left*) normalized flux (*middle*) of S II ($\lambda\lambda 1250, 1253$), Si IV ($\lambda\lambda 1393, 1402$), and C IV ($\lambda\lambda 1548, 1550$) against the LSR velocity toward each sample sightline. The H I 21 cm brightness temperature profile, $T_b(v)$, and the $N_a(v)$ profiles of the S II, Si IV, and C IV transitions are shown in the right panel. In the top right corner, we present the sightline’s name and Galactic coordinates. In the left and middle panels, we mark the absorption from the local gas centered at $v = 0 \text{ km s}^{-1}$ by the black-dash line. In the middle and right panels, the blue-dash lines indicate the adopted Perseus velocity range for each ion (see Table 2), with the blue shaded region indicating the systematic uncertainties on the velocity upper bound, v_2 .

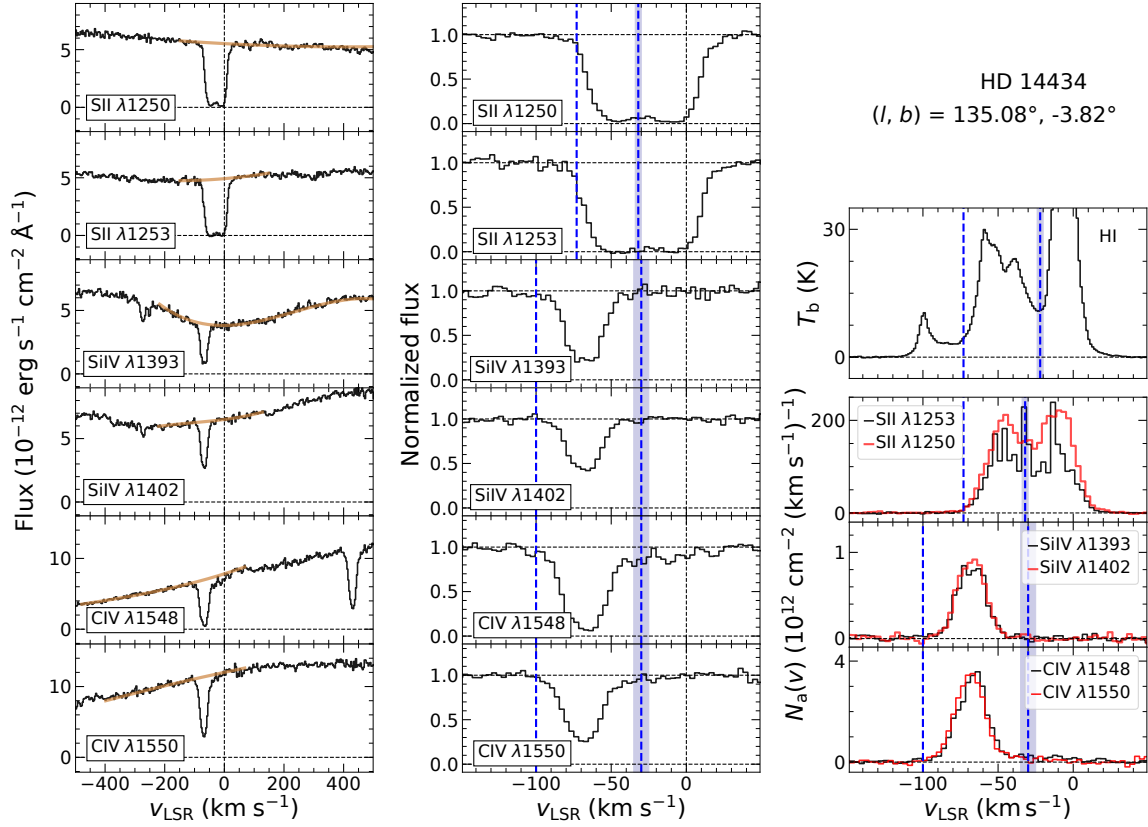


Figure 15. Same as Figure 3, *left*: raw flux with continuum models; *middle*: normalized flux, and *right*: H I 21 cm brightness temperature and $N_a(v)$ profiles of S II, Si IV, and C IV transitions toward each sightline. For details, see Appendix A.

B. CO-SPATIALITY OF S II AND C IV

In Figure 16, for each sightline, we compare the C IV $N_a(v)$ profile to the S II profile scaled down by the average C IV/S II value estimated over the Perseus velocity range for that sightline. As in Figure 4, we find that the scaled S II and C IV $N_a(v)$ profiles kinematically follow each other very well only in the disk-halo interface but very different in the thin disk. This reinstates a physical association between the highly ionized and S II bearing gas in the disk-halo interface below the Perseus arm (see Section 5.1 for more details).

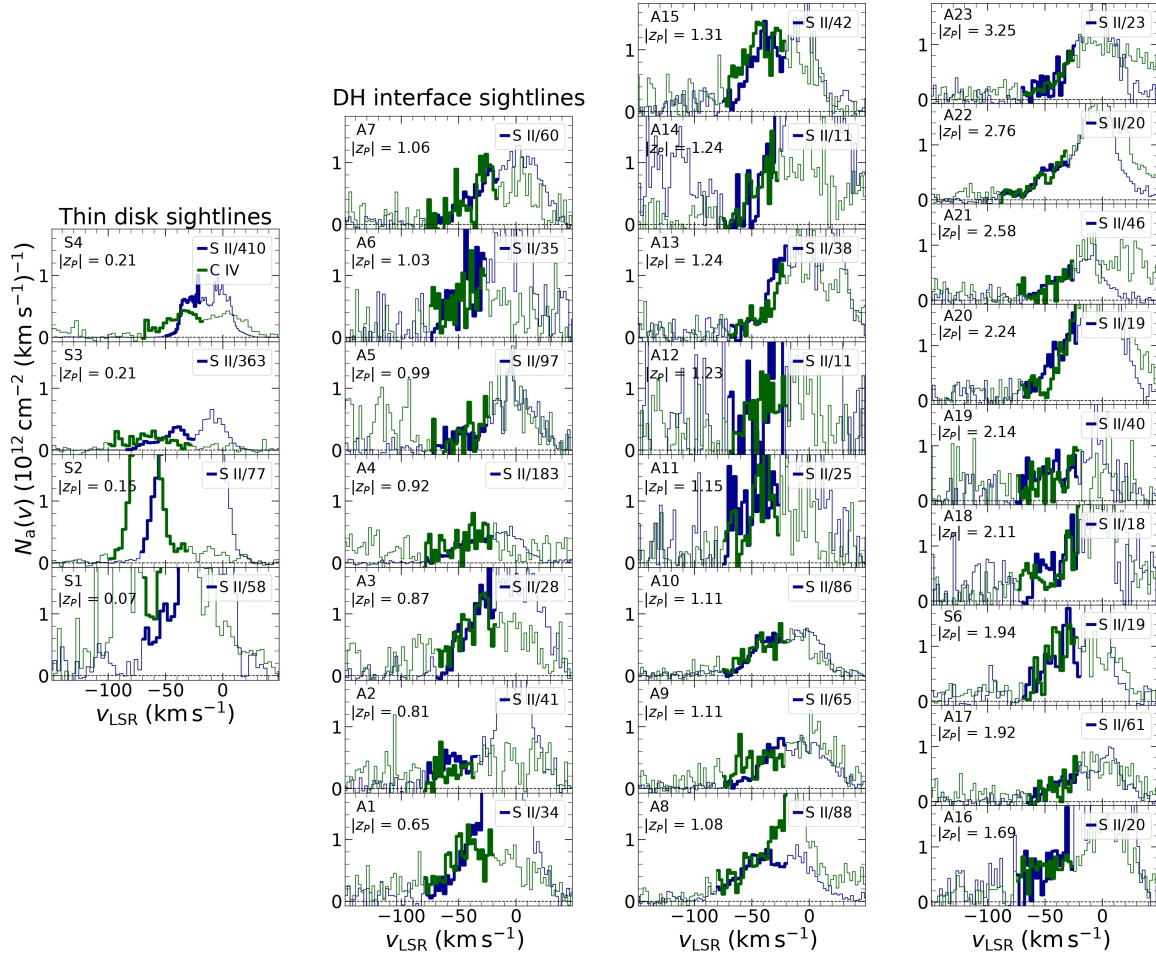


Figure 16. Same as Figure 4 and 5, toward each sightline, we compare the C IV (green) $N_a(v)$ profile to the S II (blue) profile scaled down by the average C IV/S II value estimated over the Perseus velocity range for that sightline.